PALEOENVIRONMENTS AND GEOCHRONOLOGY OF THE EOCENE WAGON BED FORMATION, CENTRAL WYOMING

By Emma E. Palko

A Thesis

Submitted in Partial Fulfillment

of the Requirements for the Degree of

Master of Science

in Geology

Northern Arizona University

May 2023

Approved:

Michael Elliot Smith, Ph.D., Chair

Ryan Porter, Ph.D.

Christine Regalla, Ph.D.

ABSTRACT

PALEOENVIRONMENTS AND GEOCHRONOLOGY OF THE EOCENE WAGON BED FORMATION, CENTRAL WYOMING

EMMA E. PALKO

The subduction of an oceanic plateau and consequent shallow subduction of the Farallon plate beneath North America have long been proposed to explain the contractile deformation that led to the formation of the Rocky Mountains and associated basins across a craton. However, questions remain about the extent of emplacement, timing of slab removal, and its influence on the land surface above. In this study, I investigate the Eocene Wagon Bed Formation in central Wyoming to better understand the relationship between its lacustrine deposits and late-stage Laramide tectonics and magmatism, as well as to provide a comprehensive record of deposition in the region during the Eocene. Eight new $^{40}Ar/^{39}Ar$ radioisotopic dates for tuff beds and volcaniclastic sandstone reveal the Wagon Bed Formation was likely deposited between 50 and 35 Ma, on far longer timescales than previously recognized, and includes a ~5 Ma unconformity in the middle. Geochronology at Lysite Mountain suggest deposition occurred only from 50 to ~43 Ma. The formation shows significant spatial and temporal variation along the Beaver Rim, with lacustrine paleoenvironments confined to the west of the Conant Creek anticline, and well-drained volcaniclastic-rich alluvial environments to the east. Similar lacustrine lithofacies to the Beaver Rim area also exist in the north at Lysite Mountain. Stable isotope data from carbonates and volcanic glass suggest the paleolakes in both locations were likely closed or semi-closed, consistent with saline lake indicators such as stromatolites, oil shales, and authigenic zeolites. Deposition of the Wagon Bed Formation suggests the collapse of the Granite Mountains began by at least 45 Ma, 30 million years earlier than currently documented. The removal of compressional

stresses during rollback caused the Granite Mountains, a rootless uplift, to extend along preexisting thrust faults or create new normal faults. Evidence of drainage disruption, lacustrine sequences, an increase in volcaniclastic material, unconformities, and extension indicate that the Wagon Bed Formation could record the surficial expression of Farallon plate removal on the overriding North American plate.

ACKNOWNLEDGEMENTS

I am endlessly grateful for the support I have received during the completion of this project, and through my career as a student. I want to thank all of my parents and grandparents for their exuberant love and encouragement to pursue my interests. I am thankful to my brother for always reminding me of home. And I would especially like to thank Andrew for reminding me there is more to life than this thesis. Furthermore, I owe much of my growth as a geologist to my advisor Dr. Michael Smith. His valuable advice and assistance have played a crucial role in shaping this project into something that I am immensely proud of.

TABLE OF CONTENTS

1. INTRODUCTION 1
1.1 Geologic Setting 1
1.2 Study Area 5
2. METHODS 6
2.1 Field area 6
2.2 Stratigraphy and Sampling 7
2.3 Gamma Ray Spectrometry 7
2.4 Geochronology 8
2.5 Stable Isotope Geochemistry 9
2.5.1 Carbonate 9
2.5.2 Volcanic Glass 9
3. RESULTS 10
3.1 Lithofacies Observations 10
3.2 Lithofacies Associations 17
3.3 Gamma Ray Assays 18
3.3.1 Observations 18
3.3.2 Interpretations 19
3.4 Geochronology Results 20
3.5 Stable Isotope Results 24
3.6 Depositional Intervals 25
4. DISCUSSION 27
4.1 Spatial and Temporal Variation 27
4.2 Surface record of Farallon plate removal 31
4.3 Range collapse 34
5. CONCLUSION 36
6. REFERENCES 39

LIST OF TABLES

Table 1. Locations of stratigraphic sections……. 49

Table 2. Lithofacies summary…….. 50

Table 2. Summary of single crystal $^{40}Ar/^{39}Ar$ dates……. 51

Table 3. Full $^{40}Ar/^{39}Ar$ single crystal results…… 52

Table 4. Oxygen and carbon stable isotope results…….. 62

Table 5. Deuterium isotope results……... 63

Table 6. Previously published dated samples of the Wagon Bed Formation……63

Table 7. Dated volcanic samples in the region……..64

LIST OF FIGURES

Figure 1. Regional location figure…… 65

Figure 2. Lithostratigraphic relationships of the Wagon Bed Formation……. 65

Figure 3. Field area location figure……... 66

Figure 4. Comparison of Wagon Bed Formation to formations in other basins……... 67

Figure 5. Lithofacies images……..... 68

Figure 6. Stratigraphic correlation at Lysite Mountain …… 69

Figure 7. Stratigraphic correlation at the Beaver Rim…….. 70

Figure 8. $^{40}Ar/^{39}Ar$ cumulative probability diagrams …….. 71

Figure 9. Sand Draw 3 measured section……. 72

Figure 10. Stable isotope fractionation figure……..…… 73

Figure 11. Stable isotope cross-plots…… 73

Figure 12. Chronostratigraphic figure of the Wagon Bed Formation……... 74

Figure 13. Synoptic paleogeographic maps of the Lysite Mountain and Beaver Rim areas…..... 75

Figure 14. Uplift collapse of the Granite Mountains ……... 76

LIST OF PLATES

Plate 1. Full correlation of measured sections along Beaver Rim and Lysite Mountain.

1. INTRODUCTION

Shallowing of the Farallon plate beneath North America due to the subduction of an oceanic plateau has long been proposed to explain contractile deformation that led to the Rocky Mountains and associated basins (Coney and Reynolds, 1977; Dickinson and Snyder, 1978; Dickinson et al., 1988; Humphreys, 2009; Liu et al., 2010; Heller and Liu, 2016), but questions remain about the extent of emplacement, timing of slab removal, and its influence on the land surface above. This project investigates the Eocene Wagon Bed Formation of central Wyoming (Fig. 1) to a) determine the relationship between its lacustrine deposits and late-stage Laramide tectonics and magmatism, and b) provide detailed stratigraphy and a comprehensive record of paleoenvironments in this region during the Eocene. I present detailed stratigraphy, new $^{40}Ar/^{39}Ar$ radioisotopic ages, stable isotopic data for regional and global comparison, constraints on relative Eocene topography, drainages disruptions, volcanism, and kinematics, all of which are related to the trajectory of the flat slab.

1.1 Geologic Setting

The Laramide Orogeny represents the end-stage of ~100 million years of Mesozoic and Cenozoic eastward subduction and contractile deformation that built the North American Cordillera (DeCelles, 2004). During the late Cretaceous through early Eocene time, the portion of the Farallon plate that was beneath present-day southern California shallowed in dip, possibly due to the subduction of the conjugate Shatsky Rise, a large oceanic plateau (Stock and Molnar, 1988; Saleeby, 2003; Humphreys, 2009; Liu et al., 2010; Heller and Liu, 2016; Copeland et al., 2017). This oblique northeast subduction and shallowing of the Farallon plate is hypothesized to have created the unique stress regimes responsible for focused Laramide contraction ~1000 km inboard of the trench, including formation of Precambrian basement arches and the creation of broad

lacustrine basins across the foreland of the North American Cordillera (Fig. 1; Coney and Reynolds, 1977; Hansen, 1984; Sales, 1984; Beck et al., 1988; Erslev, 1993; Saleeby, 2003; DeCelles, 2004; English and Johnston, 2004). Low angle subduction of the Farallon plate shut off Sierra Nevada volcanism, and continental arc magmatism migrated continentward in front of the shallow plate (Coney and Reynolds, 1977; Saleeby, 2003).

Late-stage Laramide tectonic models are debated, as the precise timing and extent of Eocene Farallon plate kinematics is unclear (Humphreys, 2009; Liu et al., 2010; Jones et al., 2011; Fan and Carrapa, 2014; Cassel et al., 2018; Carrapa et al., 2019). Removal of the Farallon plate has been interpreted by researchers to have occurred as early as the Paleocene, and as late as the Miocene (Coney and Reynolds, 1977; Humphreys, 1995; Fan and Carrapa, 2014; Smith et al., 2014; Copeland et al., 2017; Cassel et al., 2018; Currie and Copeland, 2022). Coney and Reynolds (1977) and Humphreys (1995) invoke trenchward migrating volcanism to support a 45–15 Ma and 50–20 Ma time interval, respectively, for removal from Wyoming to southern Nevada. Fan and Carrapa (2014) describe a 2-stage uplift signal in Wyoming consistent with slab emplacement from 71–58 Ma, followed by a slab removal from 58–50 Ma. Smith et al. (2014) interpret a 53–47 Ma timing for removal from Wyoming, followed by complete removal southward by ~35 Ma. Copeland et al. (2017) and Currie and Copeland (2022) use geodynamic models informed by surficial data to depict slab rollback from 55–30 Ma.

Surficial evidence evoked to describe plate removal include the cessation of contractile deformation and erosional exhumation of basement-involved uplifts (Dickinson et al., 1988; Fan and Carrapa, 2014; Copeland et al., 2017), basin subsidence (Fan and Carrapa, 2014), drainage disruption and an inception of internally drained basins (Smith et al., 2014, 2017; Canada et al., 2021), initiation of magmatism accompanied by uplift and unconformities (Coney and Reynolds,

1977; Humphreys, 1995, 2009; Smith et al., 2014; Copeland et al., 2017; Cassel et al., 2018), and extension (Constenius, 1996; Cassel et al., 2018; Canada et al., 2021). Surficial deformation of the overriding plate may occur due to slab suction above the slab hinge of the subducting plate and/or coupling of the subducting and overriding plates which facilitates surface subsidence followed by rebounding isostatic uplift (Liu et al., 2010; Heller and Liu, 2016) as warm asthenosphere moves in and thermally expands the lithosphere. Delamination of the mantle lithosphere may also contribute to dynamic uplift of the upper plate (Meissner and Mooney, 1998; Condie, 2011). Additional supporting evidence for this process includes δD paleoelevation data from hydrated volcanic glass of the Nevada hinterland which indicates that regional extension and an increase in elevation was partially driven by slab removal (Cassel et al., 2018). Furthermore, a 53-43 Ma southwest trenchward migration of magmatism from South Dakota to Utah provides the best evidence for the location of the mantle wedge during that time (Coney and Reynolds, 1977; Dickinson and Snyder, 1978; Humphreys, 1995; Saleeby, 2003; Smith et al., 2014; Behr and Smith, 2016). In summary, slab removal-induced surficial changes are hypothesized to include: 1) cessation of contractile deformation 2) ponding caused by slab suction and plate coupling-driven subsidence, followed by 3) a magmatism flare-up, 4) uplift and unconformites as hot asthenosphere moves into the space previously occupied by the cool flat slab and 5) extension and creation of normal faults.

Middle to late Eocene sedimentary strata from the post-contractional phase of the Laramide orogeny are sparse within the Laramide foreland, owing to a long period of nondeposition (Love and Christiansen, 1985; Dickinson et al., 1988; Smith et al., 2014) and post-Miocene erosion of units that may have existed (Love, 1970; McMillan et al., 2006). Early Eocene strata of the Wind River, Green River, Wasatch, and Willwood formations are well preserved within Laramide

basins, indicating primary accumulation was focused in structural lows and basin centers. In contrast, the erosional remnants of the Wagon Bed Formation occur on or adjacent to structural highs of the Wind River and Big Horn basins. This suggests either the deposits within the basin centers have since been completely eroded, or instead, deposition was focused primarily along the flanks of the Granite Mountains and Owl Creek basement uplifts.

An episode of late Oligocene and Miocene extension along uplifts across Wyoming and Utah has been hypothesized to be induced by the isostatic collapse of "rootless" Laramide arches along pre-existing crustal weaknesses in absence of dynamic compression (Sales, 1984; Hall and Chase, 1989; Aslan et al., 2017). Documented examples include the Browns Park graben of the eastern Uinta Uplift (25 Ma), the Granite Mountains (Miocene–), Owl Creek Mountains (post-Laramide), and the southern Wind River Uplift (Miocene–Pliocene) (Hansen, 1984; Sales, 1984; Hall and Chase, 1989; Prothero et al., 2008; Anders et al., 2009; Aslan et al., 2017). This process is hypothesized to be associated with the removal of Laramide compressive stresses (Sales, 1984; Hall and Chase, 1989; Weil et al., 2016) perhaps during slab removal. In these cases, because Laramide structures are proposed to be lithospheric-scale folds which displace the Moho upwards (Erslev, 1993; Tikoff and Maxson, 2001), thrust and high-angle strike-slip faults that facilitated folding during Laramide contraction may subsequently be reactivated as normal faults (Hansen, 1984; Sales, 1984; Erslev, 1993). Accommodation created within and along the margins of these collapsed features allowed sediments to accumulate and record this subsidence (Hansen, 1984; Aslan et al., 2017). Based on the proximity to the collapsed Granite and Owl Creek Mountains, the Wagon Bed Formation could similarly record uplift collapse during the Eocene, 30 million years earlier than previously documented (Love, 1970; Sales, 1984; Anders et al., 2009). Early

collapse would provide additional evidence for the timing of slab removal, and provide a mechanism for the rearrangement of paleodrainages.

1.2 Study Area

The Wagon Bed Formation (WBF) crops out along the northern and southern edges of the Wind River Basin adjacent to the Owl Creek and Granite Mountains (Fig. 1). The WBF lies conformably above the Wind River Formation and disconformably below the White River Formation. Since it was named by Franklyn Van Houten in 1964, only a limited number of detailed studies have been conducted on this interval presumably due to 1) the absence of oil-bearing units and mammalian faunas, 2) its remote location with sparse and unmaintained roads, and 3) frequent cover and slumps, which obscure unit relationships. Previous authors have interpreted the WBF to be middle to late Eocene in age (Fig. 2) based on Bridgerian through Uintan mammalian faunas (Yen, 1948; Tourtelot, 1957; Van Houten, 1964; Bay, 1969; Love, 1970; Emry, 1975; Boles and Surdam, 1979; Henrici and Fiorillo, 1993; Robinson et al., 2004) and K-Ar dates ((Love, 1964; Evernden et al., 1964). Authors describe the presence of gastropods, pelecypods, horse teeth, fish scales and turtle bones, (Yen, 1948; Van Houten, 1964; Emry, 1975; Henrici and Fiorillo, 1993). Van Houten (1955, 1964) subdivided the WBF "rather arbitrarily" into discontinuous lithologic units: gravels, sands, and muds at the base, laminated carbonate mudstones and oil shales in the middle, then volcaniclastic deposits at the top (Love, 1964, 1970; Van Houten, 1964; Bay, 1969; Baughman, 1988). Some WBF beds contain abundant authigenic clay minerals such as clinoptilolite, montmorillonite, and K-feldspar, as well as other secondary zeolites which have been interpreted to form in saline-alkaline waters (Van Houten, 1964; Bay, 1969; Boles and Surdam, 1979). However, these strata have proven hard to correlate and interpret stratigraphically. For simplicity, this study includes the uppermost volcanic sequence, which was previously

assigned to either the White River Formation (Van Houten, 1964; Love, 1970) or its own unit, the Volcanic Breccia Conglomerate (Emry, 1975; Baughman, 1988), to the upper interval of the Wagon Bed Formation (Fig. 2).

WBF strata occur adjacent to two Precambrian-cored Laramide uplifts. They share similarities with nearby Green River Formation deposits in SW Wyoming including lake facies and interbedded volcanics (Smith et al., 2008, 2014). Eocene volcanism from the Rattlesnake Hills Volcanic Province and the Absaroka Volcanic Province likely contributed the majority of volcanic sediments (Fig. 4; Hiza, 1999; Feeley and Cosca, 2003; Smith et al., 2008). These fields provide dateable materials for geochronology and are the primary evidence suggesting the contemporaneous location of the mantle wedge at the time of deposition. WBF strata record middle to late Eocene deposition, a period for which minimal records exist across the region (Love, 1964; Love and Christiansen, 1985, 1993; Dickinson et al., 1988). Deposition during this time period is important for detailed climate records during the post-Paleocene-Eocene thermal maximum phase and expansion of Antarctic ice sheets (Zachos et al., 2001; Westerhold et al., 2020). Along the southern Wind River Basin, the Conant Creek anticline — a north trending extension of Laramide-age Granite Mountains uplift — divides the WBF into east and west depositional zones (Fig. 3). Zeolite minerals consistent with authigenesis in saline lake waters occur only in the west Beaver Rim suggesting distinct and separate depositional conditions on either side of the structure created by variations in sediment delivery, evaporation, and hydrology (Boles and Surdam, 1971, 1979).

2. METHODS

2.1 Field area

The WBF was investigated at the Beaver Rim escarpment along the southern Wind River Basin, and at Lysite Mountain on the north side of the Owl Creek Mountains. (Fig. 1). Data from

legacy stratigraphy from the Lysite Mountain region (Bay, 1969), including measured sections and field observations, was incorporated into this study. At the Beaver Rim escarpment, this study's primary field site, I personally conducted field observations and collected samples for analysis. The WBF is exposed to varying extents along the escarpment and is bisected approximately in half by the Laramide-aged Conant Creek Anticline, creating west and east depositional zones (Fig. 3). This study focused on two primary sites; Sand Draw in the west, and Gas Hills in the east (Fig. 3). Due to the nature of the slumpy and frequently covered intervals of the WBF, the Sand Draw and Gas Hills localities provided notable exposures for measurement.

2.2 Stratigraphy and Sampling

I measured eight decimeter-scale stratigraphic sections for a total of 405 m to characterize sedimentary lithofacies and the depositional environment of the WBF (Table 1; Fig. 3). Gamma-ray response was recorded every 0.5 m using a portable handheld radiation spectrometer. I measured four stratigraphic sections in the west at Sand Draw and old Highway 287, and collected carbonate samples at each occurrence. In the east at Gas Hills, I measured four stratigraphic sections and collected nine volcanic tuff samples. Carbonate was absent in the east field area.

Sediment cover and poor exposure often obscured finite formation boundaries between the WBF, the lower Wind River Formation, and the upper White River Formation; however, unique marker beds allowed for sufficient internal correlation across sections of the WBF.

2.3 Gamma Ray Spectrometry

To quantitatively assess vertical variations in clay content within each stratigraphic section, a handheld gamma ray radiation spectrometer, the Radiation Solutions RS-230, was used to measure concentrations of direct radiation every 0.5 m for each stratigraphic section. The spectrometer measures radioactivity in a 1 meter diameter hemisphere for 60 seconds and returns

four values: total direct radiation (μR/hr); ^{40}K (wt.%); ^{238}U (ppm); and ^{232}Th (ppm) (Radiation Solutions Inc., 2013). Instrument calibration was conducted by recording three initial and final measurements at a control location each day. Naturally emitted measured gamma ray concentrations of K, U, and Th typically reflect the provenance, grain size, mineralogy, diagenesis, and mineralization of the lithologic material (Poupon et al., 1970; Martinius et al., 2002; IAEA, 2003; Burton et al., 2014; Moskalewicz et al., 2022). Other factors include weathering (Chan et al., 2007) and lacustrine minerals (Burton et al., 2014; Reijmer et al., 2022).

2.4 Geochronology

To assess and improve geochronological control for the WBF, ash bed samples were processed in NAU's geochronology lab following the methods outlined in Smith et al. (2003). Sanidine crystals 63–250 μm in diameter were separated through a process of crushing, sieving, and acid leaching with dilute HCl and HF to remove the aggregate and clays. Sanidine crystals were then handpicked under a microscope using refractive-index oils, then washed in acetone and ethanol to remove the oil residue. Once separated, viable samples were sent to the University of Wisconsin-Madison's WiscAR lab to obtain laser-fused single-crystal dates using a gas source mass spectrometer. Single crystal dates ensure that xenocrysts or crystals with diffusion loss do not contaminate the date. The crystals were sent to the Oregon State University's Radiation Center to be co-irradiated with the Fish Canyon Tuff sanidine standard of 28.201 Ma (Kuiper et al., 2008), then returned to the WiscAr lab and placed into the mass spectrometer with the Fish Canyon Tuff sanidine to obtain precise dates. All ages are reported with 2σ uncertainties relative to the 28.201 age for Fish Canyon sanidine standard ((Kuiper et al., 2008) using the decay constants of Min et al. (2000).

2.5 Stable Isotope Geochemistry

Stable isotopic analysis of carbonate and volcanic glass was completed to access lake water evaporation and concentration evolution through time.

2.5.1 Carbonate

Carbonate is prevalent throughout the WBF west of the Conant Creek anticline, including carbonate cemented tuff and limestone. However, east of the anticline in the Gas Hills region, carbonate is notably absent. In the field, 25 total carbonate samples were collected in the Sand Draw region at each stratigraphic occurrence. In preparation for stable isotope analysis, each sample was hammered to expose unweathered surfaces and powdered using a corundum mortar and pestle. Analysis was completed at The University of Kansas W.M. Keck NSF Paleoenvironmental and Environmental Stable Isotope Laboratory using a Thermo Kiel IV Carbonate device connected to a Thermo Finnigan MAT 253 stable isotope ratio mass spectrometer. Stable isotope values $\delta^{18}O$ and $\delta^{13}C$ are reported relative to V-PDB, Vienna Pee Dee belemnite, in per mil (‰). The precision for $\delta^{18}O$ and $\delta^{13}C$ of each sample is $\leq$0.5‰ and $\leq$0.4‰, respectively.

2.5.2 Volcanic Glass

In windward continental interiors, the primary control of the δD value of meteoric water is elevation (Dansgaard, 1964; Cassel et al., 2018). As air masses condense over high topography, successive precipitation events remove the heavier Deuterium ion, leading to Deuterium depletion with elevation (Dansgaard, 1964; Rowley, 2007; Cassel et al., 2018); Meteoric δD glass give values of -158‰ to -160‰ across the Eocene Cordillera (Smith et al., 2017; Cassel et al., 2018); however, once on Earth's surface, ponded meteoric water is modified by evaporation, which enriches the δD value of lake waters when flow through the system is low, as evaporated water

has low D/H ratios (Dansgaard, 1964; Cassel et al., 2018). Lake-evaporated δD values range from -60‰ to -100‰ (Smith et al., 2017; Cassel et al., 2018). δD enrichment in lacustrine waters provides a measure of lake evaporation and concentration through time, and is the primary use for this study.

To identify the δD value of meteoric water within the WBF, pure volcanic glass from tuffaceous material was analyzed for hydrogen isotopic ratios. Post-deposition, volcanic glass hydrates with meteoric water over 10^3 to 10^4 years (Cassel and Breecker, 2017) and then develops a nanoporous silica-rich layer on the exterior which resists additional hydration or isotopic exchange, preserving the paleo-meteoric δD values (Cassel and Breecker, 2017; Cassel et al., 2018). Three tuffaceous samples collected from the east Beaver Rim, 2 collected from the west Beaver Rim, and one collected at Lysite Mountain were analyzed by the University of Idaho Tectonics and Basin Analysis lab.

3. RESULTS

3.1 Lithofacies Observations

Lithofacies of the WBF are identified and described. A summary of these nine lithofacies including descriptions, characteristics and interpreted depositional environments are given as follows (Table 2).

Tuffaceous Sandstone (Lf-1): The tuffaceous sandstone lithofacies is very fine to medium-grained, moderately to well-sorted, often biotite-rich sandstone, with predominantly quartz and feldspar phenocrysts in an ashy matrix (Fig. 5). Beds of tuffaceous sandstone contain horizontal bedding, parallel and wavy lamination, normal grading, or may be structureless. Paleosol development is present in several beds, with horizons of brown waxy, iron-rich, ped-like structures. Ash-filled

root traces and vertical burrows are observed in the paleosol horizons. Beds are typically gray to tan in color.

Interpretation: The fine to medium-grained horizontal bedding, parallel laminations, root traces, and weak paleosol development indicate that the tuffaceous sandstone accumulated in a floodplain environment (Nanson and Croke, 1992; Kraus and Gwinn, 1997; Miall, 2010; Colombera and Mountney, 2019). The finest-grained successions likely accumulated on the floodplain, whereas coarser grains may be a part of the point bar, overbank, or crevasse splay deposits (Bridge, 1984; Nanson and Croke, 1992). The ashy matrix suggests that windblown volcanic ash was deposited on the floodplain surface and was subsequently reworked and mixed with existing sand and mud grains. Ash-filled root traces are tabular and do not penetrate deeply, indicating that the floodplain may have been saturated during periods of time (Retallack, 1988). Additionally, previous researchers have noted the presence of authigenic zeolite minerals within tuffaceous beds containing altered volcanic glass, including clinoptilolite, heulandite, chabazite, montmorillonite, analcime, and potassium feldspar (Boles and Surdam, 1971, 1979). Clinoptilolite, heulandite, and potassium feldspar, which only form in lacustrine settings, occur exclusively west of the Conant Creek Anticline where ponding occurred (Boles and Surdam, 1979).

Sandstone (Lf-2): This lithofacies consists of fine to coarse-grained sandstone with infrequent granule and pebble-sized clasts (Fig. 5). It ranges from poorly to well sorted, and contains little to no tuffaceous material. Sand grain lithology consists of subrounded quartz, feldspar, muscovite, and dark black grains. These beds contain 1–3 cm scale cross-bedding, horizontal bedding, are frequently normally graded, or are structureless. Beds of this lithofacies are more resistive than others, contributing to frequent outcrops.

Interpretation: The range in grain size from fine to coarse, 1–3 cm cross-bedding, and normal grading suggest that the sandstone lithofacies was deposited in laterally accreting point bars within a shallow fluvial channel (Nanson and Croke, 1992; Miall, 2010). The lack of tuffaceous material suggests the mud-sized ash particles remained in suspension and were washed downstream while larger sand grains remained in the bed load.

Tuffaceous mudstone (Lf-3): This lithofacies is clay-rich with fine to medium-grained phenocrysts in a mud-sized ashy matrix (Fig. 5). Phenocrysts include biotite and quartz grains. Many of the tuffaceous mudstone beds are crumbly, flaky, and heavily weathered at the surface. Horizontal laminations and weak paleosol development with brown waxy peds are present. The mudstone is brown to gray in color, but weathers to white at the surface in some cases. Tuffaceous mudstone makes up the majority of the recessive units within the stratigraphy and is frequently covered.

Interpretation: The presence of horizontal laminations, sand-sized phenocrysts, and weak paleosol development suggests that the tuffaceous mudstone lithofacies was deposited in a floodplain via overbank deposition (Bridge, 1984; Nanson and Croke, 1992; Kraus and Gwinn, 1997). The ashy matrix, in addition to biotite and quartz phenocrysts, indicates air fall ash was deposited and incorporated into the floodplain deposits. The weak development of paleosol horizons and regular incorporation of this lithofacies into overlying beds of Lf-8, indicate that stream avulsions and/or crevasse splay deposits are frequent and energetic (Kraus and Gwinn, 1997).

Pebble Conglomerate (Lf-4): The pebble conglomerate lithofacies is a matrix-supported conglomerate with very coarse to pebble-sized clasts predominantly of quartz and feldspar up to 4–6 cm in diameter (Fig. 5). Clasts are subrounded to rounded, and beds are unsorted to moderately

sorted. Beds contain horizontal bedding, local 5–10 cm scale cross-bedding, and weak normal grading in some cases. Beds may grade into Lf-2.

Interpretation: Considering the rounded gravel-sized clasts, 5–10 cm cross-bedding, and normal grading, I interpret the pebble conglomerate lithofacies to be deposited near the base of a fluvial channel and along point bar lateral accretion surfaces (Miall, 1977, 2010).

Carbonate-cemented sandstone (Lf-5): This lithofacies is very fine to medium-grained, with biotite, quartz, and feldspar grains (Fig. 5). Beds are cemented with carbonate and may contain iron staining or iron mottling. Tuffaceous material is a common constituent, in the form of an ashy matrix. Beds of this lithofacies can contain 1–4 cm thick horizontal bedding, wavy lamination, or may be structureless.

Interpretation: Carbonate cement, horizontal bedding, laminations, and fine ashy matrix suggest this lithofacies was deposited in a mixed setting, either on a floodplain or in a shallow lacustrine environment. Finely laminated beds, interbedded with fine ash may have been deposited in a shallow lacustrine or palustrine setting (Renaut and Gierlowski-Kordesch, 2010), while coarser-grained beds may have accumulated carbonate through carbonate-rich groundwater fluids in the soil (Zamanian et al., 2016). Furthermore, because pedogenic carbonate forms when evapotranspiration exceeds precipitation (Zamanian et al., 2016), beds of pedogenic carbonate may have formed during dry periods, while beds with lacustrine carbonate formed during wet periods when a paleolake was able to inundate the locality. Additionally, the presence of zeolite minerals in many beds of this lithofacies, noted by previous researchers Boles and Surdam (1971, 1979), is interpreted to represent deposition in a mildly alkaline lake (<9 pH) due to the presence of calcium

carbonate and the absence of saline minerals (eg. trona) (Mariner and Surdam, 1970; Boles and Surdam, 1979).

Sandy limestone (Lf-6): This lithofacies is light gray in color, with beds ranging from 2–20 cm thick, and has a high proportion of siliciclastic sand grains, typically clear or dark in color. Several beds contain thin laminations of calcite. The Sand Draw 3 stratigraphic section contains a prominent stromatolite bed, with individual stromatolites ranging in size from 5–30 cm tall (Fig. 5). Fossil allochems are absent.

Interpretation: Bedding thickness variation, presence of siliciclastic material, calcite laminations, and a stromatolite bed indicate that this lithofacies was deposited in a shallow lacustrine environment (Renaut and Gierlowski-Kordesch, 2010; Martin-Bello et al., 2019). Sand grains from the surrounding area were washed in and delivered by streams. The stromatolites in this lithofacies resemble the thin planar stromatolites with undulatory or gently convex laminae of Martin-Bello et al. (2019), which form in a moderate energy, shallow water environment, with moderate to high sediment supply. Furthermore, the paleolake during stromatolite growth was likely mildly saline-alkaline (Awramik and Buchheim, 2015) and lacked grazing or burrowing invertebrates (Garrett, 1970).

Mudstone (Lf-7): Mudstone is tan to brown, has fine horizontal laminations, and is frequently interbedded with very fine-grained tuffaceous material (Fig. 5). This lithofacies is infrequently observed in outcrop, as it is recessive, highly weathered, and likely underlies many covered sections.

Interpretation: Based on the fine mud-sized laminations, in which tuffaceous material is commonly interbedded, I interpret this lithofacies as deposited in a shallow lacustrine environment

(Renaut and Gierlowski-Kordesch, 2010). Energy levels were low, allowing mudstone to accumulate, and suspended air fall ash to settle to the bottom.

Intraclastic reworked tuff (Lf-8): The intraclastic reworked tuff lithofacies has a very fine to fine-grained ashy matrix with biotite, quartz, and feldspar phenocrysts (Fig. 5). It contains 0.5–3 cm clasts of iron-rich mudball intraclasts, incorporated from the underlying bed. These mudballs are normally graded within the beds and are not typically present at the top of the bed. These beds are up to 4.5 m thick, are generally poorly sorted and unstructured with a distinctive nodular appearance, and only contain faint evidence of internal organization. Some beds include subtle 0.5 m scale cross-bedding and truncation along the upper boundary. This is a unique lithofacies that is laterally continuous across several kilometers and is used as a marker bed for section correlations.

Interpretation: Given the thickness of beds, ashy matrix, mud intraclasts, mild internal organization, and lateral continuity, I interpret this lithofacies to be the result of thick air fall volcanic ash reprocessed in a floodplain environment (Kataoka and Nakajo, 2002; Sohn and Sohn, 2019). The mud intraclasts, integrated mainly from Lf-3, indicate that this ash flowed over a floodplain and incorporated clasts of unlithified soil and mud. Subtle 0.5 m cross-bedding suggests the ash was able to flow and organize internally, perhaps by overbank channel flow (Bridge, 1984). Ash that fell into the channels may have been subsequently incorporated into beds of Lf-1. Authigenic zeolite minerals have not been identified in these beds by this study or by previous authors.

Volcanic pebble conglomerate (Lf-9): This lithofacies is a poorly sorted matrix-supported pebble conglomerate with 2% granule, 92% pebble, and 6% cobble-sized clasts. The matrix consists of

fine to medium-grained ash and sand grains and is cemented with carbonate (Fig. 5). The clasts are subrounded to rounded, with lithologies of 45% granite, 16% mudball, 11% quartz, 11% andesite, 8% gabbro, 3% quartzofeldspathic, and <1% of intraclast, gneiss, gabbro, volcanic breccia, rhyolite, sandstone, granodiorite, quartzite, and diorite. Beds with 2–15 cm scale cross-bedding are present, often with truncated tops and undulatory erosive lower bedding surfaces. Horizontal lamination, wavy lamination, normal grading, and inverse grading are commonly present. Some beds show faint westward imbrication of pebble-sized clasts.

Interpretation: Considering this lithofacies has large rounded clasts of varying lithologies, is matrix-supported with an ashy groundmass, and is erosive at lower bedding surfaces, I interpret the depositional mechanism to be a combination of type-1 and type-2 lahars or debris flows deposited within a broad paleochannel (Major, 2022). Type-1 lahars are a mixture of approximately equal sediment and water, are poorly sorted, can move a range of sediment sizes from mud to boulder (Major, 2022), and represents the coarsest-grained beds. Cross-bedded lenses of mostly matrix material may have been deposited in type-2 lahar sequences, where the flow has a higher proportion of water than sediment (Major, 2022). Outcrops of this lithofacies were named "volcanic breccia conglomerate" and described by Baughman (1988) as interbedded laharic and fluvial sequences. However, these beds are far more organized than expected for a volcanic debris flow, and include highly rounded clasts indicative of turbulent flow, not laminar. Baughman (1988) mapped a unit composed of this lithofacies to be an independent stratigraphic unit separate from the underlying WBF and the overlying White River Formation. This study includes this lithofacies in the WBF.

3.2 Lithofacies Associations

Lithofacies Association 1 (LA1) - Fluvial: This association includes tuffaceous sandstone (Lf-1), sandstone (Lf-2), tuffaceous mudstone (Lf-3), pebble conglomerate (Lf-4), and carbonate cemented sandstone (Lf-5) (Table 2). It is predominantly composed of well-bedded mudstones, sandstones, and conglomerates deposited in various fluvial and floodplain environments. Sand and gravel were transported and organized by channels, point bars, and overbank flow (Bridge, 1984; Retallack, 1988; Nanson and Croke, 1992; Kraus and Gwinn, 1997; Miall, 2010; Colombera and Mountney, 2019). Windblown volcanic ash is commonly reprocessed by existing stream channels and modified on the floodplain by soil formation. Root traces and paleosol development indicate stable vegetated floodplains were common (Retallack, 1988).

Lithofacies Association 2 (LA2) - Lacustrine: This association includes carbonate cemented sandstone (Lf-5), sandy limestone (Lf-6), and mudstone (Lf-7) (Table 2). Dominant beds are finely laminated mud, stromatolites, limestone or carbonate cemented beds, deposited in, or on the margins of a shallow lake (Renaut and Gierlowski-Kordesch, 2010). Stable isotope analyses of carbonate samples indicate periods of increased evaporation and organic burial over time. The sandy, thin, and planar stromatolite beds are evidence of moderate energy at the lacustrine margin with notable sediment input (Martin-Bello et al., 2019). Finely laminated mudstone indicates a calmer environment near the depositional center of the paleolake.

Lithofacies Association 3 (LA3) - Volcaniclastic: This association includes intraclastic reworked tuff (Lf-8) and volcanic pebble conglomerate (Lf-9) (Table 2). Both facies are the result of volcanic material that has been transported, reorganized, and deposited by a fluvial mechanism (Major, 2022). These depositional events are extreme, drastically modify the existing landscape, and have

the ability to be laterally continuous for 10's of kilometers. Rounded clasts vary in size from mud to cobbles, indicating high energy flow capable of transporting clasts long distances.

3.3 Gamma Ray Assays

3.3.1 Observations

Gamma ray measurements of naturally emitted radiation concentrations of K (wt.%), U (ppm), and Th (ppm) within a bed are traditionally used as a lithologic proxy for grain size due to the greater concentrations of these elements in clay minerals (Poupon et al., 1970; Martinius et al., 2002; Burton et al., 2014; McGowin, 2015; Moskalewicz et al., 2022). However, the measurements recorded along the Beaver Rim do not consistently follow this simple relationship, therefore requiring additional interpretation.

In the west Beaver Rim, total direct radiation values are primarily controlled by variations in K values. Average values in this area for K, U, and Th are 2.8 wt.%, 4.3 ppm, and 11.5 ppm, respectively (Plate 1). In Sand Draw 1 and Sand Draw 3, elevated K values of 4–6 wt.% clearly define two distinct intervals of deposition (Plate 1). U and Th values are slightly elevated in these sections but are not significantly higher than baseline values. Total direct radiation values in the east Beaver Rim are primarily controlled by variations in U and Th, with only minor variations in K. Average values in this area for K, U, and Th are 2.2 wt.%, 6.2 ppm, and 20.9 ppm, respectively (Plate 1). Th values show significant variability, with frequent and major excursions of up to 30 ppm above the baseline values of 12–16 ppm. K values show significantly more variations in the west, while U and Th values are distinctly elevated in the east.

3.3.2 Interpretations

Elevated K values may be the result of 2 factors: 1) progressive concentration of lacustrine waters, which increases K concentration allowing autogenic clay minerals to incorporate more K into its structure (Deocampo, 2015), and 2) a high proportion of detrital minerals rich in potassium feldspars, micas, and clay minerals such as illite (Fabricius et al., 2003) in sandstone and clay sediments delivered from the Granite Mountains and Rattlesnake Hills volcanics. Lacustrine concentration is favored for elevated K in West Beaver Rim, while the concentration of K-bearing minerals in sandstones may explain high values in the east.

Elevated U values may be the result of 3 factors: 1) the uranyl ion (UO^{2+}) creates ionic complexes with carbonate within organic matter which may concentrate U in beds with high total organic content (Martinius et al., 2002; Fabricius et al., 2003), 2) delivery of U rich accessory minerals, such as zircon, monazite, and apatite, via detritus from the Granite Mountains and or Rattlesnake Hills (Fabricius et al., 2003), and 3) preferential adsorption and concentration of U onto clay minerals and in soils (Dickson and Scott, 1997; Fabricius et al., 2003; McGowin, 2015). Organic matter concentration is favored in the west during periods of lacustrine deposition, while delivery of high U detritus and concentration in soils is favored for elevated U in the east.

Elevated Th values may be the result of 3 factors: 1) due to its insolubility, Th may concentrate in residual deposits such as clays (Fabricius et al., 2003), 2) detrital minerals concentrated in Th, such as monazite, zircon, and allanite, eroded and delivered from granite of the Granite Mountains or from volcanics of the Rattlesnake Hills (Martinius et al., 2002; Fabricius et al., 2003), and 3) adsorption of Th to clay minerals (Martinius et al., 2002; Fabricius et al., 2003) and accumulation in paleosols during continental oxidizing conditions (Martinius et al., 2002). Given that the highest Th values are in the east, which is most proximal to Granite Mountain

exposures and Rattlesnake Hills volcanic vents, detrital delivery of Th-bearing minerals is favored for elevated Th in the east, while clay mineral adsorption and paleosol concentration may explain small Th excursions in the west.

3.4 Geochronology Results

A total of 8 volcanic tuff samples were analyzed using $^{40}Ar/^{39}Ar$ laser fusion sanidine. Ages for these units are based on weighted means of laser-fused sanidine dates. Five unimodal populations are present, and three samples yielded more complicated populations. All are reported with 2σ uncertainties relative to the 28.201 Ma age for Fish Canyon tuff sanidine (Kuiper et al., 2008). Single crystal ages were omitted from the weighted mean age calculation on the basis of interpreted age scatter, generally contamination from detrital or xenocrystic sources, or anomalously low radiogenic argon (<95% $^{40}Ar^*$). The mean squared weighted deviates (MSWD) was used to assess the scatter of the data around the weighted mean age. When the MSWD was greater than 1, the analytical error was multiplied by the square root of the MSWD. Table 3 includes a summary of these results, including full uncertainties which include decay constant and primary standard uncertainty. Table 4 reports the complete $^{40}Ar/^{39}Ar$ results for each sample.

442WB: This sample was collected near Lysite Mountain, at the Hawkes Butte measured section of Bay (1969). The sampled bed is approximately 5 meters above the base of the section (Fig. 6), and 20 of 33 grains yielded a weighted mean age of 50.32 ± 0.08 Ma (MSWD = 1.01) (Fig. 8). The remaining 13 grains were omitted for the following reasons: 6 grains yielded Precambrian-Devonian ages and are interpreted to be detrital grains from exposures of strata of these ages in the nearby Owl Creek Mountains; 7 grains yielded Cretaceous ages between 94-101 Ma indicating

Sierra Nevada sourced sanidine (Fiske and Tobich, 1994; DeCelles and Graham, 2015; Schwartz, 2021) eroded from Cretaceous-age formations also exposed in the Owl Creek Mountains.

445WB: This sample was collected near Lysite Mountain, at the Hawkes Butte measured section of Bay (1969). The sampled bed is approximately 20 meters above the base of the section (Fig. 6). Only 1 out of 30 grains yielded an Eocene age, which I interpret as a maximum depositional age (MDA) for this bed. The interpreted MDA for this single grain is 50.05 ± 0.15 Ma (Fig. 8). The remaining 29 grains are older than Eocene and are excluded based on their age: 9 grains yielded Precambrian ages and 10 grains yielded Cambrian-Jurassic all interpreted as detrital grains from exposures of strata of this age in the nearby Owl Creek Mountains; 7 grains yielded Cretaceous ages between 94–101 Ma indicating Sierra Nevada sourced sanidine (Fiske and Tobich, 1994; DeCelles and Graham, 2015; Schwartz, 2021) eroded from Cretaceous-age strata also exposed in the Owl Creek Mountains.

447WB: This sample was collected near Lysite Mountain, at the Hawkes Butte measured section of Bay (1969). The sampled bed is approximately 30 meters above the base of the section (Fig. 6). The youngest of 31 grains from this sample has a single grain age of 45.15 ± 0.07 Ma (Fig. 8), which is interpreted to be the best estimate of the maximum depositional age. The remaining 30 grains were omitted because they exhibit < 95% ^{40}Ar*, suggestive of significant daughter loss which would yield an inaccurate age.

450WB: This sample was collected from the WBF along the west Beaver Rim. The sampled bed is from the Sand Draw 1 stratigraphic section, at approximately 52 m from the base (Fig. 7), is 2.5 meters thick, biotite rich, shows no signs of placering or alteration, and represents the tuffaceous sandstone lithofacies. A total of 19 out of 33 grains were used to calculate a weighted mean age of

39.84 ± 0.09 Ma (MSWD = 1.54) (Fig. 8). The remaining 13 grains were omitted for the following reasons: 5 grains yielded Precambrian ages, interpreted as detrital grains from Precambrian exposures in the Granite Mountains; 1 grain yielded a Permian age, interpreted to be a detrital grain from Permian formations exposed in anticlines along the Granite Mountains or on the flanks of the Wind River Mountains; 8 grains had < 95% ^{40}Ar*, suggestive of daughter loss, and were excluded from the weighted mean age calculation.

451WB: This was collected from the WBF along the west Beaver Rim. The sampled bed is from the Sand Draw 1 stratigraphic section, at approximately 67 m above the base (Fig. 7), is 10 meters thick, light tan to buff-colored, carbonate cemented, and is represented by the carbonate cemented sandstone lithofacies. A total of 21 out of 30 grains were used to calculate a weighted mean age of 35.68 ± 0.06 Ma (MSWD = 1.22) (Fig. 8). The remaining 9 grains were omitted for the following reasons: 1 grain as an early Eocene age of 52.8, interpreted as a xenocryst or detrital grain from Eocene strata exposed nearby; 1 grain yielded a Cretaceous age, interpreted as a xenocryst or detrital grain from Cretaceous strata exposed in anticlines along the Granite Mountains or on the flanks of the Wind River Mountains; 7 grains range from 35.8–36.2 Ma, are older than the single population which yielded the interpreted age and may be xenocrysts..

452WB: This sample was collected from the WBF along the west Beaver Rim. This sample does not fall within a stratigraphic section, but was collected at the top of the tuffaceous bed of sample 451WB. A total of 17 out of 35 grains were used to calculate a weighted mean age of 35.68 ± 0.06 Ma (MSWD = 1.27) (Fig. 8). The remaining 18 grains were omitted for the following reasons: 3 grains had < 95% ^{40}Ar*, suggesting daughter loss and were excluded from the weighted mean age calculation; 14 grains are older than the single population which yielded the interpreted age; 1

grain gave an age that is an outlier from the interpreted population age, has 95.5% ^{40}Ar*, and may represent daughter loss.

Given samples 451WB and 452WB-B were sampled from the same bed, a two-tailed t-test was completed to determine statistical similarity. This test yielded a P value of 0.568, a t Stat value of -0.575, and a two-tailed critical value of 2.028. The P value is greater than the standard significance level of 0.05, and the t Stat value is less than the critical value. Therefore the null hypothesis, that the samples are statistically similar, is not rejected. Data from both samples were pooled to calculate a single weighted mean age. 21 grains of sample 451WB were combined with 17 grains of sample 452WB-B to yield a weighted mean age of 35.68 ± 0.02 Ma (MSWD = 1.2).

W33: This sample was collected from the WBF along the east Beaver Rim. The sampled bed is from the Gas Hills 4 stratigraphic section, at approximately 58 m above the base (Fig. 7), is 2 meters thick, light gray with biotite grains, and is represented by the tuffaceous sandstone lithofacies. The 9 youngest grains out of 20 were used to calculate a weighted mean age of 46.92 ± 0.06 Ma (MSWD = 1.33) (Fig. 8). The remaining 11 grains were omitted because they are older than the single population which yielded the interpreted age and are interpreted to be xenocrysts or detrital.

W34: This sample was collected from the WBF along the east Beaver Rim. The sampled bed is from the Gas Hills 4 stratigraphic section, at approximately 59 m above the base (Fig. 7), is 1 meters thick, light gray with biotite grains, and is represented by the intraclastic reworked tuff lithofacies A total of 4 out of 28 grains were used to calculate a weighted mean age of 46.76 ± 0.07 Ma (MSWD = 0.19) (Fig. 8). The remaining 24 grains were omitted for the following reasons: The youngest grain has <95% ^{40}Ar*, suggesting daughter loss and was excluded from the weighted

mean age calculation; 3 grains are older than the single population which yielded the interpreted age and are interpreted to be xenocrysts or detrital; 20 grains range from Cretaceous to Precambrian in age and are interpreted to be detrital grains from strata exposed in the Granite Mountain area, or are xenocrysts.

3.5 Stable Isotope Results

Oxygen Isotopes: $\delta^{18}O$ values of carbonates from the WBF along the west Beaver Rim vary between -18.63‰ and -1.36‰, and have an average of -10.52‰ with a standard deviation of 5.44‰ (Table 5). The record exhibits two enriched sections, with values of -5‰ or greater (Fig. 9), separated by depleted values of -10‰ or less. Enrichment of $\delta^{18}O$ values in these carbonate beds may represent increased evaporative concentration of ^{18}O during these periods of deposition, likely in a closed or semi-closed lacustrine setting (Fig. 10) (Oberhänsli and Allen, 1987; Talbot, 1990; Cohen, 2003; Leng and Marshall, 2004; Deocampo, 2010). Depleted $\delta^{18}O$ values may represent an influx of unevaporated meteoric water to the paleolake (Leng and Marshall, 2004) or drier periods during which pedogenic carbonate, instead of lacustrine carbonate, was precipitated (Deocampo, 2010; Horton et al., 2016).

Carbon Isotopes: $\delta^{13}C$ values of carbonate in WBF samples vary between -5.54‰ and 2.16‰, and have an average of -2.67‰ with a standard deviation of 2.10‰ (Table 5). Similar to $\delta^{18}O$, the $\delta^{13}C$ record exhibits two enriched sections, with values of -2‰ or greater (Fig 8), separated by depleted values of -2‰ or less. Enrichment of $\delta^{13}C$ values in these carbonate beds may represent increased productivity, burial, and preservation of organic material (Cohen, 2003; Leng and Marshall, 2004; Deocampo, 2010) due to periods of lake stratification (Cohen, 2003), or may indicate the presence of carbonate in the catchment area (Fig. 10; Leng and Marshall, 2004). $\delta^{18}O$ and $\delta^{13}C$ closely

covary (Figs. 9; 11) which may indicate periods of basin closure (Talbot, 1990); however, this relationship may only be robust for long-lived closed basins (Drummond et al., 1995; Li and Ku, 1997; Leng and Marshall, 2004).

Hydrogen Isotopes: δD values from 6 samples across the Beaver Rim are given in Table 6. Samples 444WB from Lysite Mountain and White Lignitic Tuff from the west Beaver Rim are enriched with δD values of -108.37‰ and -83.59‰, respectively. This indicates periods of increased evaporation in lacustrine environments (Fig. 10). Sample 450WB from the west Beaver Rim has a depleted value of -160.05‰, indicating that evaporation did not modify meteoric water at this stratigraphic occurrence. Three samples from the east Beaver Rim show no evidence of evaporation, with very depleted δD values of –181.81‰, –193.96‰, and –168.44‰. This indicates that east Beaver Rim was well drained and not ponded during the deposition of these three tuffaceous samples. Drainage may have flowed westward toward the ponded basin along the west Beaver Rim, but the absence of paleoflow indicators makes it difficult to determine the direction of drainage with any certainty.

3.6 Depositional Intervals

The WBF can be subdivided into five depositional intervals in the Beaver Rim area using data obtained in this study in conjunction with previously published data (Figs. 5; 11; Plate 1). These intervals differ from the units described by Van Houten (1964), as this study's intervals account for additional information other than just lithology. Stratigraphic correlations were made using marker beds that were traceable laterally, similarities in lithofacies characteristics, gamma ray characteristics, and radioisotopic ages. The duration of each depositional interval was estimated using radioisotopic ages near the base and top of the WBF, and documented mammalian

fossils (Fig. 12; Van Houten, 1964; Robinson et al., 2004; Lucas et al., 2004). Although many beds from the lower half of the WBF have been dated (Table 7), these beds do not fall within a measured section, preventing precise age constraints on lacustrine deposition; therefore, intervals 1-4 are divided equally in time.

Interval 1 – Fluvial (50.5– 49 Ma): This interval includes the lowermost WBF and is conformable with the underlying fluvial Wind River Formation. This interval is characterized by sandstones and mudstones deposited in a floodplain or in fluvial channels, and was deposited between 50–49 Ma.

Interval 2 – Lacustrine (49–47.5 Ma): This interval is only present in west Beaver Rim, and is characterized by lacustrine lithofacies with enriched $\delta^{18}O$, $\delta^{13}C$, and δD values, and elevated K wt.% gamma ray values. Previous authors have indicated the presence of freshwater gastropods, catfish and garpike scales, and zeolitized minerals (Van Houten, 1964; Boles and Surdam, 1979). Deposition occurred between 49–47.5 Ma.

Interval 3 – Fluvial (47.5–46 Ma): Interval 3 is characterized by floodplain mudstones, depleted $\delta^{18}O$ and $\delta^{13}C$ values, an absence of carbonate lithologies, and low K wt.% gamma ray values. This interval separates lacustrine Intervals 2 and 4, which suggests the paleolake experienced periods of drying and reduction in size. Deposition occurred between 47.5–46 Ma. Coeval volcaniclastic strata are deposited within the floodplain at the east Beaver Rim.

Interval 4 - Lacustrine (46–44.5 Ma): As Interval 2, this interval is only present in west Beaver Rim, contains lacustrine lithofacies, enriched $\delta^{18}O$, $\delta^{13}C$, and δD values, and elevated K wt.% gamma ray values. A prominent stromatolite bed and finely laminated mudstones are present. Previous authors have indicated the presence of freshwater gastropods, catfish and garpike scales,

and zeolitized minerals (Van Houten, 1964; Boles and Surdam, 1979). Deposition occurred between 46–44.5 Ma. Coeval volcaniclastic strata are deposited within the floodplain at the east Beaver Rim.

Interval 5 - Volcanic/Fluvial (40–35 Ma): This interval is characterized by an erosive lower bedding surface, dominantly volcanic lithologies, and stable and low gamma values which contrast the varied gamma ray values in Intervals 1–4. An unconformity exists between Interval 4 and Interval 5 and represents nondeposition between 44.5–40 Ma (Fig. 12). Deposition of Interval 5 occurred between 40–35 Ma. The overlying White River Formation cut channels into this upper interval.

4. DISCUSSION

4.1 Spatial and Temporal Variation

The findings of this study indicate that the WBF records several terrestrial depositional environments and indicates a much longer-lived WBF along the Beaver Rim than was previously recognized. New $^{40}Ar/^{39}Ar$ radioisotopic dates and legacy geochronology for the WBF show that deposition likely started around 50 Ma and lasted until 35 Ma, punctuated by an unconformity at both the Beaver Rim and Lysite Mountain (Tables 3; 7; Fig. 12). These dates show that deposition occurred at Lysite Mountain from 50–43 Ma. At the Beaver Rim, deposition was likely quasi-continuous from 50–44.5 Ma, after which deposition ceased until 40 Ma and then persisted until at least 35 Ma.

The WBF crops out on the flanks of the east-west trending Owl Creek Mountains and along the northern edge of the Granite Mountains. Because significant late-Miocene erosion has occurred in many basins of the Laramide Foreland (Blackwelder, 1915; Keefer, 1970; Love, 1970; Trimble, 1980; McMillan et al., 2006), it is difficult to say whether these sections of the WBF were ever

connected. Both locations share many lithologic and stratigraphic similarities suggesting similar depositional environments existed in both places; however these environments are not exactly correlative in time. To highlight the spatial and temporal similarities and differences between the WBF near Lysite Mountain and at the Beaver Rim, synoptic paleogeographic maps were created for descriptions of both locations at 54, 50, 46, 42, 38, and 34 Ma (Fig. 13).

54 Ma

Fluvial deposition of the early Eocene Wind River Formation was dominant within the Wind River Basin at this time (Keefer, 1970; Love, 1970). Fluvial channels were directed eastward (Fig. 13).

50 Ma

Lysite Mountain: An angular unconformity exists between Mesozoic strata – including Cody Shale and Chugwater Formations – and the base of the WBF (Bay, 1969). By this time, deposition was well underway (Fig. 13). Lithologies here include sandstones, mudstones, distorted oil shales, carbonaceous beds, and zeolitized tuffaceous beds (Love, 1964; Bay, 1969). These lithologies indicate that lacustrine deposition was dominant at this time, and the presence of enriched δD values (Table 6), oil shales, and zeolites suggest this lacustrine basin was likely closed, stratified, and at least mildly saline (Bay, 1969; Mariner and Surdam, 1970). The spatial extent of this paleolake is poorly understood due to a lack of study and subsequent erosion of much of the WBF in the Big Horn and Wind River basins (Love, 1964), but likely coincides with existing outcrops (Bay, 1969). It is possible that it was once connected to the Beaver Rim paleolake, but there is currently a lack of evidence to support or refute this idea.

Beaver Rim: WBF deposition has just begun after 4 myr of Wind River Formation alluvial deposition (Fig. 13; Keefer, 1970). The environment is entirely fluvial with Interval 1 deposition of mudstones in the floodplains, and sandstones and gravels in river channels. Here, the WBF is

conformable with the underlying Wind River Formation (Van Houten, 1964; Love, 1970), with sediment accumulation along the base of the Granite Mountains and out into the Wind River Basin.

46 Ma

Lysite Mountain: Deposition of the WBF continues here, with evidence of continued lacustrine conditions (Fig. 13; Bay, 1969). Limestone and mudstone is prevalent. One large volcanic tuff bed was dated using K/Ar and reported as 46.2 ± 1.5 Ma (Table 7; Love, 1964). However this date has not been recalibrated using current decay constants and standards, because the required data for recalibration was never published.

Beaver Rim: Deposition of the WBF has transitioned from entirely fluvial to closed or semi-closed lacustrine deposition, only in the west (Fig. 13). Zeolitized tuffaceous beds, stromatolites, finely laminated mudstones, carbonaceous beds, enriched stable isotopes, fish scales, and freshwater gastropods all indicate the presence of a lake. This lake most likely experienced periods of drying and reduction in spatial extent, evidenced by intervals of fluvial deposition between lacustrine intervals. Deposition of the WBF during this time was focused mainly at the base of the Granite Mountains instead of at the Wind River Basin depocenter, suggesting that significant drainage disruption has occurred. In some locations, especially in the east Beaver Rim, the WBF onlaps Precambrian basement exposures of the Granite Mountains (Fig. 12) instead of conformable deposition with the Wind River Formation. This uplift-focused deposition contrasts prior deposition focused in basin centers, and indicates that substantial surficial changes have occurred to make this change. Additionally, the Rattlesnake Hills Volcanic Province initiates at ~46 Ma and was only active until 45 Ma. This volcanic center supplies significant amounts of volcaniclastic detritus to both east and west of the Conant Creek Anticline.

42 Ma

Lysite Mountain: Deposition of the WBF has ceased (Fig. 13). Nondeposition continues until the Quaternary when stream channels are able to preserve alluvium (Love and Christiansen, 1985). The absence of units younger than the Wagon Bed Formation is consistent with substantial regional uplift (Keefer, 1970).

Beaver Rim: A period of nondeposition occurs during this time (Fig. 13). The absence of geochronology and biostratigraphic markers provide the best evidence for this. Additionally, an unconformity is interpreted from several measured sections, evidenced by erosive lower bedding surfaces, and a marked change in the variability of the gamma-ray measurements (Plate 1).

38 Ma

Lysite Mountain: Nondeposition continues (Fig. 13).

Beaver Rim: Following a period of nondeposition, the WBF rejuvenates and Interval 5 deposition occurs (Fig. 13). This unit is volcanic-rich and represents periods of energetic fluvial deposition. Beds of boulder-sized clasts in an ashy volcanic matrix within this upper WBF unit have been described as a lahar sequence (Baughman, 1988). Prior to this study, this uppermost portion of the WBF has been poorly constrained stratigraphically. Some authors have combined this interval with the overlying White River Formation (Van Houten, 1964; Love, 1970), while others have correlated this section to the Wiggins Formation, another volcanic formation in the area (Fig. 2; Emry, 1975; Baughman, 1988). The substantial unconformity and distinct lithologic character of this upper unit may justify the naming of a new unit; however, given its limited spatial extent and undetermined correlation to the Lysite Mountain area, I have included this unit into the WBF for simplicity.

34 Ma

Lysite Mountain: Nondeposition continues (Fig. 13).

Beaver Rim: Energetic, volcanic rich, fluvial lithofacies of the White River Formation are deposited (Fig. 13; Love, 1970). These fluvial sequences cut large substantial channels into the underlying WBF strata (Van Houten, 1964; Love, 1970) indicating that the Granite Mountains area experienced significant erosion followed by White River Formation deposition. Additional formations in the region including the Oligocene South Pass Formation of the southern Wind River Mountains (Steidtmann and Middleton, 1991) and the Bishop Conglomerate of the Uinta Mountain region (Hansen, 1984) represent a reinvigoration of sedimentation after a period of nondeposition, similar to the White River Formation at the Beaver Rim.

4.2 Surface record of Farallon plate removal

The post-contractional phase of the Laramide Orogeny is still widely debated among the geologic community, due in part to a deficiency of direct physical evidence and uncertainty over the exact timing and extent of slab removal dynamics. Several researchers have presented an upper plate deformation model to define the trajectory and timing of Farallon slab rollback (Smith et al., 2014, 2017; Cassel et al., 2018). Direct evidence for this model includes drainage disruption, closed lacustrine basins, initiation of volcanic activity, unconformities, and extension. Given the lithological characteristics, age, and location of the WBF, I propose that this formation provides additional evidence in support of this model.

Geochronologic and biostratigraphic evidence indicates that the WBF was deposited between approximately 50–35 Ma, with deposition beginning in the north near Lysite Mountain prior to 50 Ma followed closely in the south at the Beaver Rim at 50 Ma. Lacustrine deposition occurred at Lysite Mountain from 50–43 Ma and at the Beaver Rim from approximately 49–45 Ma. These lacustrine basins show evidence of closure and internal drainage suggesting that the streams and rivers, which previously fed sediment to the center of the Wind River and Big Horn

Basins from the Granite and Owl Creek uplifts, had been disrupted. These closed lacustrine basins may have formed as a result of slab-induced surface subsidence due to suction at the slab hinge as it steepens and rolls back. Alternatively, they could reflect structural partitioning of the landscape into smaller drainage basins.

A large proportion of the sediment within the WBF is volcaniclastic, indicating that volcanic centers nearby provided much of this material. The Absaroka Volcanic Province, northwest of the Wind River Basin, was active between 54–45 Ma (Table 8; Hiza, 1999; Feeley and Cosca, 2003; Smith et al., 2014) and likely was the main supplier of volcanic detritus to the Owl Creek uplift region. Additionally, the Rattlesnake Hills Volcanic Province, approximately 180 km southwest of the Absaroka Province, was active for a short period of time from 46–45 Ma (Table 8; (Pekarek, 1974; Lynds et al., 2016). This initiation of volcanism provides the most direct evidence for the location of the mantle wedge beneath the North American lithosphere during this time (Coney and Reynolds, 1977; Smith et al., 2014; Cassel et al., 2018).

The WBF records a significant unconformity after the lacustrine intervals at both the Beaver Rim and Lysite Mountain. At Lysite Mountain the unconformity occurs after approximately 43 Ma and continues until the Quaternary (Love, 1964; Love and Christiansen, 1985). At the Beaver Rim, this unconformity only lasts from approximately 44.5–40 Ma, after which the tuffaceous White River Formation is deposited broadly across the region (Love, 1964; Love and Christiansen, 1985). This gap in regional deposition was noticed by Love (1964) and Dickinson (1988) during analysis of Eocene intermontane ponded basins (Fig. 4). This unconformity may represent isostatic uplift on the order of several 100s of meters created by asthenospheric heating and delamination of the North American mantle lithosphere (Meissner and Mooney, 1998; Heller and Liu, 2016). This has been described thoroughly within the Laramide

Hinterland with the use of paleoelevations to constrain total uplift during rollback (Cassel et al., 2018).

This progression of surficial changes including lake formation, volcanism and unconformities over the course of several million years is consistent with the models proposed by Smith et al. (2014; 2017), Cassel et al., (2018), and Canada et al. (2021) for Farallon plate removal. The WBF is able to fill in gaps in the spatial distribution of Laramide Foreland sedimentation in the post-contractional phase and provides further evidence for the pattern of surficial changes the upper plate may experience due to slab rollback. However, this data presents an interesting temporal problem, as lakes and unconformities develop within the WBF at 50 Ma and 45 Ma, respectively, approximately 3 million years later than Green River Formation strata to the south (Figs. 1, 4). If these lacustrine basins develop, close, and then are uplifted in a northeast to southwest progression, WBF formation strata should show signs of this process before Green River Formation strata, not after. One possible explanation for this is the distinct difference of size and catchment area of the two basins. Because the WBF developed so closely to the Granite Mountains and Owl Creek uplifts, their response to uplift may not have developed as quickly, since drainages into the ponded areas were limited.

Some researchers have proposed alternate theories to describe Laramide deformation seen on the surface of the North American plate. These theories include Farallon plate slab tear along the northwest margin beneath Idaho (Humphreys, 1995, 2009), the accretion of Shatsky conjugate depleted mantle lithosphere beneath Wyoming (Humphreys et al., 2015), and a collision and translation of an insular terrane along the western Laurentian margin (Maxson and Tikoff, 1996; Tikoff et al., 2023). Because a Farallon plate slab tear and accretion of depleted mantle lithosphere

beneath North America are not mutually exclusive of a northeast to southwest removal of the subducted flat slab, the WBF cannot differentiate between these alternatives.

4.3 Range collapse

The Granite Mountains once had as much relief as other Laramide uplifts within Wyoming (Keefer and Love, 1963; Love, 1970); however, only remnants of these basement-cored peaks remain today. This uplift collapse has been documented to have occurred along the North and South Granite Mountain Faults (Weil et al., 2016) during at least the Miocene, based on a similar case of collapse in the eastern Uinta uplift (Hansen, 1984; Sales, 1984; Aslan et al., 2017), regional southward dip of Miocene and Pliocene strata (Love, 1970), and ages of tephra deposits of 11–6 Ma within the Moonstone Formation against basement exposures (Fig 12; Love, 1970; Anders et al., 2009; Heller et al., 2011). However, I propose that two pieces of evidence from the WBF suggest that the Granite Mountain collapse began in the Eocene.

The first piece of evidence is a proposed change of primary deposition of the WBF from basin centers in Depositional Interval 1 to uplift adjacent lacustrine deposition in Intervals 2–5. This contradicts the typical depositional model of lacustrine basins that usually form at the bottom of the landscape. Instead, sediments up to 200 meters thick were deposited at the base of the Granite Mountains, indicating that accommodation must have been present for deposition to occur in this location (Van Houten, 1964). Moreover, channelized beds containing rounded cobbles and boulders within Depositional Interval 5 have been documented as a lahar derived from the Absaroka Mountains to the northeast (Baughman, 1988). Given the distance of travel, the energy necessary to transport material of this size, and close proximity to a longstanding depositional basin, it is unusual that this sediment would accumulate near the base of a mountain range instead of the basin. This starkly contrasts early deposition of the WBF, which includes erosional remnants

of the Granite Mountains itself. Due to late-Miocene erosion of the Wind River Basin sediments, a Granite Mountain adjacent depositional center for the WBF is not certain; however, future work correlating subsurface thicknesses of the WBF just south of the Beaver Rim escarpment may contribute insights.

The second piece of evidence supporting the early onset of the Granite Mountain collapse is the onlap of the WBF on Precambrian exposures of the Granite Mountains in the east Beaver Rim (Fig. 12). Published ages of the WBF from this location are between 48–45 Ma (Table 7). This suggests that the formation was filling low areas around the core and margins of the Granite Mountains within the Eocene, which could only happen if the topography was low in those areas. Therefore, I suggest that the region near the Granite Mountains had developed into a basin capable of sediment deposition and transport by at least 45 Ma (Fig. 12). This timing of Granite Mountain collapse is far more consistent with extensional basin formation and Cordillera collapse documented to have begun by 49-48 Ma (Constenius, 1996), than extension in the Miocene.

Average orientations of Laramide-aged basement structures, folds, and faults trend northwest indicating a SW-NE vergent paleo stress field (Erslev, 1993). This stress field produced connected anastomosing arches surrounded by large disconnected elliptical basins (Erslev, 1993). Computer models using structural, paleomagnetic, and stress data produce models in support of this stress field (Bird, 1988, 1998). Unlike the NW-SE trending Laramide arches the Wind River, Big Horn and Laramie mountains, the Granite and Owl Creek mountains trend approximately E-W. Uplifts of their basement cores relied upon sinistral and dextral oblique thrust faults (Molzer and Erslev, 1995; Weil et al., 2016) which bounded the ranges (Fig. 14). This transpression created rootless uplifts which lacked support from the underlying crust (Sales, 1984; Hall and Chase, 1989; Erslev, 1993; Weil et al., 2016; Aslan et al., 2017). Once compressional stress was removed as the

slab began to roll back, high topography began to collapse along pre-existing faults, or created new ones (Fig. 14; Hansen, 1984; Sales, 1984; Thompson, 2015; Weil et al., 2016). The existence of WBF deposits along these collapsed structures contributes to the approximate timing of range collapse and potentially provides additional evidence of Farallon slab removal prior to 45 Ma.

5. CONCLUSION

In the first detailed stratigraphic study of the Wagon Bed Formation in over 50 years, 8 new $^{40}Ar/^{39}Ar$ radioisotopic dates, comprehensive lithologic examinations, regional correlations, gamma-ray surveys, stable isotopic data, and a thorough account of previously published data, allow for the following interpretations of this formation.

1. Geochronologic evidence presented here indicates that the WBF was deposited between approximately 50–35 Ma. This suggests deposition on far longer timescales than previously known and provides a record of deposition during a time period in which minimal records exist. Other deposits in this region aged 45–35 Ma are noticeably absent or have since been eroded away.

2. Significant spatial and temporal differences exist for the depositional environments of the WBF across the Beaver Rim. In the west, stromatolites, carbonaceous beds, laminated mudstones, enriched δD, and $\delta^{18}O$ values, documented zeolite minerals — especially lacustrine phases such as clinoptilolite, heulandite, and K-feldspar — and fossils such as freshwater gastropods, catfish, and garpike scales, indicate that a lake was present in the west. However, in the east a lack of carbonate, significantly depleted δD values, and no lake lithologies suggest the environment was likely a well-drained floodplain.

3. The WBF deposits near the Owl Creek Mountains share many similarities with deposits along the Beaver Rim but initiated earlier. Published data indicates the presence of lacustrine sequences, evidenced by carbonaceous shale and siltstone, and fish fossils. Additionally, evidence

such as oil shales, zeolitized tuffaceous sediments, and undisturbed sediment varves further suggest that the lake was stratified and likely saline. Geochronologic evidence from this location indicates lacustrine deposition had begun by 50 Ma and only continued until ~43 Ma.

4. Lacustrine sediments at the Beaver Rim and at Lysite Mountain accumulated in a closed or semi-closed basin. This is evidenced by a) δD and $\delta^{18}O$ enrichment at the Beaver Rim, indicating periods of increased evaporation, b) authigenic zeolites in both locations such as clinoptilolite, heulandite, and K-feldspar, which only form in saline lacustrine settings, c) the presence of finely laminated mud, oil shales, and stromatolites which only form in lacustrine waters which are saline and stratified, and d) high K wt.% values of gamma-ray measurements in the west Beaver Rim which further reflect the presence of authigenic clay minerals. Drainage reorganization and disruption likely contributed to the creation of these paleolakes.

5. Deposition of the WBF potentially records the surficial expression of Farallon plate rollback on the overriding North American plate. First, the transition from deposition primarily in the center of the Wind River and Big Horn basins to uplift-adjacent deposition suggests significant drainage disruption and reorganization. Additionally, the presence of closed lacustrine basin formation, followed by volcanism, and a large unconformity marks the time of initial surficial drawdown due to suction at the slab hinge, followed by uplift when the asthenosphere moves into the space previously occupied by the subducted slab. This creates isostatic uplift from heating and delamination. Furthermore, the inception of Rattlesnake Hills volcanism at 46–45 Ma provides the strongest evidence for the location of the asthenospheric wedge at that time.

6. Evidence from the WBF suggests that the collapse of the Granite Mountains began by at least 45 Ma, while previous research suggests that the collapse only occurred during the Miocene. Once a significant Laramide uplift, only remnants remain of the Granite Mountains due

to collapse along the North and South Granite Mountain Faults. Two key pieces of supporting evidence include a transition from basinal WBF deposition to uplift-adjacent deposition, and onlap of WBF onto Precambrian basement of the Granite Mountains. As the Farallon slab rolled back, removal of compressional stress caused this rootles uplift to extend along preexisting thrust faults or create new ones. The existence of WBF deposits along these collapsed structures constrains the timing of range collapse and provides additional evidence of Farallon slab rollback.

6. REFERENCES

Anders, M.H., Saltzman, J., and Hemming, S.R., 2009, Neogene tephra correlations in eastern Idaho and Wyoming: Implications for Yellowstone hotspot-related volcanism and tectonic activity: GSA Bulletin, v. 121, p. 837–856, doi:10.1130/B26300.1.

Aslan, A., Boraas-Connors, M., Sprinkel, D.A., Becker, T.P., Lynds, R., Karlstrom, K.E., and Heizler, M., 2017, Cenozoic collapse of the eastern Uinta Mountains and drainage evolution of the Uinta Mountains region: Geosphere, v. 14, p. 115–140, doi:10.1130/GES01523.1.

Awramik, S.M., and Buchheim, H.P., 2015, Giant stromatolites of the Eocene Green River Formation (Colorado, USA): Geology, v. 43, p. 691–694, doi:10.1130/G36793.1.

Baughman, R.L., 1988, Sedimentology of an eocene volcanic mudflow deposit, Beaver Rim, Fremont County, Wyoming [PhD Thesis]: Northern Arizona University.

Bay, K.W., 1969, Stratigraphy of Eocene sedimentary rocks in the Lysite Mountain area, Hot Springs, Fremont, and Washakie counties, Wyoming [PhD Thesis]: University of Wyoming, http://search.proquest.com/dissertations-theses/stratigraphy-eocene-sedimentary-rocks-lysite/docview/302362644/se-2.

Beck, R.A., Vondra, C.F., Filkins, J.E., and Olander, J.D., 1988, Syntectonic sedimentation and Laramide basement thrusting, Cordilleran foreland; Timing of deformation:, doi:10.1130/MEM171-p465.

Behr, W.M., and Smith, D., 2016, Deformation in the mantle wedge associated with Laramide flat-slab subduction: Geochemistry, Geophysics, Geosystems, v. 17, p. 2643–2660, doi:10.1002/2016GC006361.

Bird, P., 1988, Formation of the Rocky Mountains, Western United States: A Continuum Computer Model: Science, v. 239, p. 1501–1507, doi:10.1126/science.239.4847.1501.

Bird, P., 1998, Kinematic history of the Laramide orogeny in latitudes 35°-49°N, western United States: Tectonics, v. 17, p. 780–801, doi:10.1029/98TC02698.

Blackwelder, E., 1915, Post-Cretaceous History of the Mountains of Central Western Wyoming: The Journal of Geology, v. 23, p. 193–217.

Boles, J.R., and Surdam, R.C., 1971, Authigenesis of the Wagon Bed Formation, central Wyoming: Rocky Mt Geol., https://pubs.geoscienceworld.org/uwyo/rmg/article-pdf/10/2/141/2950865/141.pdf.

Boles, J.R., and Surdam, R.C., 1979, Diagenesis of volcanogenic sediments in a Tertiary saline lake; Wagon Bed Formation, Wyoming: American Journal of Science, v. 297, p. 832–853.

Bridge, J.S., 1984, Large-scale facies sequences in alluvial overbank environments: Journal of Sedimentary Research, v. 54, p. 583–588, doi:10.1306/212F8477-2B24-11D7-8648000102C1865D.

Burton, D., Woolf, K., and Sullivan, B., 2014, Lacustrine depositional environments in the Green River Formation, Uinta Basin: Expression in outcrop and wireline logs: AAPG Bulletin, v. 98, p. 1699–1715, doi:10.1306/03201413187.

Canada, A.S., Cassel, E.J., and Smith, M.E., 2021, Geochemical Evolution of Eocene Lakes in the Nevada Hinterland of the North American Cordillera: Geochemistry, Geophysics, Geosystems, v. 22, p. e2021GC009863, doi:10.1029/2021GC009863.

Carrapa, B., DeCelles, P.G., and Romero, M., 2019, Early Inception of the Laramide Orogeny in Southwestern Montana and Northern Wyoming: Implications for Models of Flat-Slab Subduction: Journal of Geophysical Research: Solid Earth, v. 124, p. 2102–2123, doi:10.1029/2018JB016888.

Cassel, E.J., and Breecker, D.O., 2017, Long-term stability of hydrogen isotope ratios in hydrated volcanic glass: Geochimica et Cosmochimica Acta, v. 200, p. 67–86, doi:10.1016/j.gca.2016.12.001.

Cassel, E.J., Smith, M.E., and Jicha, B.R., 2018, The Impact of Slab Rollback on Earth's Surface: Uplift and Extension in the Hinterland of the North American Cordillera: Geophysical Research Letters, v. 45, p. 10,996-11,004, doi:10.1029/2018GL079887.

Chan, L.S., Wong, P.W., and Chen, Q.F., 2007, Abundances of radioelements (K, U, Th) in weathered igneous rocks in Hong Kong: Journal of Geophysics and Engineering, v. 4, p. 285–292, doi:10.1088/1742-2132/4/3/S07.

Cohen, A.S., 2003, Paleolimnology: The History and Evolution of Lake Systems: Oxford University Press, 540 p.

Colombera, L., and Mountney, N.P., 2019, The lithofacies organization of fluvial channel deposits: a meta-analysis of modern rivers: Sedimentary Geology, v. 383, p. 16–40.

Condie, K.C., 2011, Chapter 7 - Crustal and Mantle Evolution, *in* Condie, K.C. ed., Earth as an Evolving Planetary System (Second Edition), Boston, Academic Press, p. 261–316, doi:10.1016/B978-0-12-385227-4.00004-3.

Coney, P., and Reynolds, S., 1977, Cordilleran Benioff zones: Nature, v. 270, p. 403–406, doi:10.1038/270403a0.

Constenius, K.N., 1996, Late Paleogene extensional collapse of the Cordilleran foreland fold and thrust belt: GSA Bulletin, v. 108, p. 20–39, doi:10.1130/0016-7606(1996)108<0020:LPECOT>2.3.CO;2.

Copeland, P., Currie, C.A., Lawton, T.F., and Murphy, M.A., 2017, Location, location, location: The variable lifespan of the Laramide orogeny: Geology, v. 45, p. 223–226, doi:10.1130/G38810.1.

Currie, C.A., and Copeland, P., 2022, Numerical models of Farallon plate subduction: Creating and removing a flat slab: Geosphere, v. 18, p. 476–502, doi:10.1130/GES02393.1.

Dansgaard, W., 1964, Stable isotopes in precipitation: Tellus, v. 16, p. 436–468, doi:10.1111/j.2153-3490.1964.tb00181.x.

DeCelles, P.G., 2004, Late Jurassic to Eocene evolution of the Cordilleran thrust belt and foreland basin system, western U.S.A.: American Journal of Science, v. 304, p. 105–168, doi:10.2475/ajs.304.2.105.

DeCelles, P.G., and Graham, S.A., 2015, Cyclical processes in the North American Cordilleran orogenic system: Geology, v. 43, p. 499–502, doi:10.1130/G36482.1.

Deocampo, D., 2015, Authigenic clay minerals in lacustrine mudstones: Special Paper of the Geological Society of America, v. 515, p. 49–64, doi:10.1130/2015.2515(03).

Deocampo, D.M., 2010, Chapter 1 The Geochemistry of Continental Carbonates, *in* Alonso-Zarza, A.M. and Tanner, L.H. eds., Developments in Sedimentology, Elsevier, Carbonates in Continental Settings: Geochemistry, Diagenesis and Applications, v. 62, p. 1–59, doi:10.1016/S0070-4571(09)06201-3.

Dickinson, W.R., Klute, M.A., Hayes, M.J., Janecke, S.U., Lundin, E.R., McKittrick, M.A., and Olivares, M.D., 1988, Paleogeographic and paleotectonic setting of Laramide sedimentary basins in the central Rocky Mountain region: GSA Bulletin, v. 100, p. 1023–1039, doi:10.1130/0016-7606(1988)100<1023:PAPSOL>2.3.CO;2.

Dickinson, W.R., and Snyder, W.S., 1978, Plate tectonics of the Laramide orogeny:, doi:10.1130/MEM151-p355.

Dickson, B., and Scott, K., 1997, Interpretation of aerial gamma-ray surveys - adding the geochemical factors: AGSO journal of Australian geology & geophysics, v. 17, p. 187–199.

Drummond, C.N., Patterson, W.P., and Walker, J.C.G., 1995, Climatic forcing of carbon-oxygen isotopic covariance in temperate-region marl lakes: Geology, v. 23, p. 1031–1034, doi:10.1130/0091-7613(1995)023<1031:CFOCOI>2.3.CO;2.

Emry, R., 1975, Revised Tertiary Stratigraphy and Paleontology of the Western Beaver Divide, Fremont County, Wyoming: Smithsonian Contributions to Paleobiology, v. 25, doi:10.5479/si.00810266.25.1.

English, J., and Johnston, S., 2004, The Laramide Orogeny: What Were the Driving Forces? International Geology Review - INT GEOL REV, v. 46, p. 833–838, doi:10.2747/0020-6814.46.9.833.

Erslev, E., 1993, Thrusts, back-thrusts, and detachment of Rocky Mountain foreland arches:, https://www.researchgate.net/publication/279723671_Thrusts_back-thrusts_and_detachment_of_Rocky_Mountain_foreland_arches (accessed March 2022).

Evernden, J.F., Savage, D.E., Curtis, G.H., and James, G.T., 1964, Potassium-argon dates and the Cenozoic mammalian chronology of North America: American Journal of Science, v. 262, p. 145–198, doi:10.2475/ajs.262.2.145.

Fabricius, I.L., Fazladic, L.D., Steinholm, A., and Korsbech, U., 2003, The use of spectral natural gamma-ray analysis in reservoir evaluation of siliciclastic sediments: a case study from the Middle Jurassic of the Harald Field, Danish Central Graben: GEUS Bulletin, v. 1, p. 349–366, doi:10.34194/geusb.v1.4677.

Fan, M., and Carrapa, B., 2014, Late Cretaceous-early Eocene Laramide uplift, exhumation, and basin subsidence in Wyoming: Crustal responses to flat slab subduction: Tectonics (Washington, D.C.), v. 33, p. 509–529, doi:10.1002/2012TC003221.

Feeley, T.C., and Cosca, M.A., 2003, Time vs. composition trends of magmatism at Sunlight volcano, Absaroka volcanic province, Wyoming: GSA Bulletin, v. 115, p. 714–728, doi:10.1130/0016-7606(2003)115<0714:TVCTOM>2.0.CO;2.

Fiske, R.S., and Tobich, O.T., 1994, Middle Cretaceous ash-flow tuff and caldera-collapse deposit in the Minarets Caldera, east-central Sierra Nevada, California: GSA Bulletin, v. 106, p. 582–593, doi:10.1130/0016-7606(1994)106<0582:MCAFTA>2.3.CO;2.

Garrett, P., 1970, Phanerozoic Stromatolites: Noncompetitive Ecologic Restriction by Grazing and Burrowing Animals: Science, v. 169, p. 171–173, doi:10.1126/science.169.3941.171.

Hall, M.K., and Chase, C.G., 1989, Uplift, unbuckling, and collapse: Flexural history and isostasy of the Wind River Range and Granite Mountains, Wyoming: Journal of Geophysical Research: Solid Earth, v. 94, p. 17581–17593, doi:10.1029/JB094iB12p17581.

Hansen, W.R., 1984, Post-Laramide tectonic histroy of the eastern Uinta Mountainsm Utah, Colorado, and Wyoming: The Mountain Geologist, https://archives.datapages.com/data/rmag/mg/1984/hansen1.pdf.

Heller, P.L., and Liu, L., 2016, Dynamic topography and vertical motion of the U.S. Rocky Mountain region prior to and during the Laramide orogeny: GSA Bulletin, v. 128, p. 973–988, doi:10.1130/B31431.1.

Heller, P., McMillan, M., and Humphrey, N., 2011, Climate-induced formation of a closed basin: Great Divide Basin, Wyoming: Geological Society of America Bulletin, v. 123, p. 150–157, doi:10.1130/B30113.1.

Henrici, A.C., and Fiorillo, A.R., 1993, Catastrophic death assemblage of Chelomophrynus bayi (Anura, Rhinophrynidae) from the Middle Eocene Wagon Bed Formation of central Wyoming: J. Paleontol., v. 67, p. 1016–1026, doi:10.1017/S0022336000025348.

Hiza, M.M., 1999, The geochemistry and geochronology of the Eocene Absaroka volcanic province northern Wyoming and southwest Montana, USA: Oregon State University.

Horton, T.W., Defliese, W.F., Tripati, A.K., and Oze, C., 2016, Evaporation induced 18O and 13C enrichment in lake systems: A global perspective on hydrologic balance effects: Quaternary Science Reviews, v. 131, p. 365–379, doi:10.1016/j.quascirev.2015.06.030.

Humphreys, E., 1995, Post-Laramide removal of the Farallon slab, western United States: Geology, v. 23, doi:10.1130/0091-7613(1995)023<0987:PLROTF>2.3.CO;2.

Humphreys, E., 2009, Relation of flat subduction to magmatism and deformation in the western USA: Geological Society of America Memoirs, v. 204, p. 85–98, doi:10.1130/2009.1204(04).

Humphreys, E.D., Schmandt, B., Bezada, M.J., and Perry-Houts, J., 2015, Recent craton growth by slab stacking beneath Wyoming: Earth and Planetary Science Letters, v. 429, p. 170–180, doi:10.1016/j.epsl.2015.07.066.

IAEA, I.A.E.A., 2003, Guidelines for Radioelement Mapping Using Gamma Ray Spectrometry Data: Guidelines for Radioelement Mapping Using Gamma Ray Spectrometry Data, https://www.iaea.org/publications/6746/guidelines-for-radioelement-mapping-using-gamma-ray-spectrometry-data (accessed January 2023).

Jones, C.H., Farmer, G.L., Sageman, B., and Zhong, S., 2011, Hydrodynamic mechanism for the Laramide orogeny: Geosphere, v. 7, p. 183–201, doi:10.1130/GES00575.1.

Kataoka, K., and Nakajo, T., 2002, Volcaniclastic resedimentation in distal fluvial basins induced by large-volume explosive volcanism: the Ebisutoge–Fukuda tephra, Plio-Pleistocene boundary, central Japan: Sedimentology, v. 49, p. 319–334, doi:10.1046/j.1365-3091.2002.00445.x.

Keefer, W.R., 1970, Structural Geology of the Wind River Basin, Wyoming: U.S. Government Printing Office, 35 p.

Keefer, W.R., and Love, J.D., 1963, Laramide vertical movements in central Wyoming: Rocky Mountain Geology, v. 2, p. 47–54.

Kraus, M.J., and Gwinn, B., 1997, Facies and facies architecture of Paleogene floodplain deposits, Willwood Formation, Bighorn Basin, Wyoming, USA: Sedimentary Geology, v. 114, p. 33–54, doi:10.1016/S0037-0738(97)00083-3.

Kuiper, K.F., Deino, A., Hilgen, F.J., Krijgsman, W., Renne, P.R., and Wijbrans, J.R., 2008, Synchronizing rock clocks of Earth history: Science (New York, N.Y.), v. 320, p. 500–504, doi:10.1126/science.1154339.

Leng, M.J., and Marshall, J.D., 2004, Palaeoclimate interpretation of stable isotope data from lake sediment archives: Quaternary Science Reviews, v. 23, p. 811–831, doi:10.1016/j.quascirev.2003.06.012.

Li, H.-C., and Ku, T.-L., 1997, δ13C–δ18C covariance as a paleohydrological indicator for closed-basin lakes: Palaeogeography, Palaeoclimatology, Palaeoecology, v. 133, p. 69–80, doi:10.1016/S0031-0182(96)00153-8.

Liu, L., Gurnis, M., Seton, M., Saleeby, J., Müller, D., and Jackson, J., 2010, The role of oceanic plateau subduction in the Laramide orogeny: Nature Geoscience, v. 3, p. 353–357, doi:10.1038/NGEO829.

Love, J.D., 1970, Cenozoic Geology of the Granite Mountains Area, Central Wyoming: geologic Survey Professional Paper,.

Love, J.D., 1964, Uraniferous phosphatic lake beds of Eocene age in intermontane basins of Wyoming and Utah: Professional Paper, v. 474-E, doi:10.3133/pp474E.

Love, J.D., and Christiansen, A.C., 1985, Geologic Map of Wyoming: U.S. Geological Survey.

Love, J.D., and Christiansen, A.C., 1993, Stratigraphic chart showing Phanerozoic nomenclature for the state of Wyoming: Geologic Survey of Wyoming Map Series 41.

Lucas, S.G., Zeigler, K.E., and Kondrashov, P.E., 2004, Late Eocene brontotheres (Mammalia, Perissodactyla) from the Beaver Divide, Wyoming, and their biochronological significance: New Mexico Museum of Natural History and Science, 227 p.

Lynds, R., Toner, R., Freye, A., Sutherland, W., and Loveland, A., 2016, Preliminary geologic map of the Ervay Basin SW Quadrangle Natrona County, Wyoming.:

Major, J.J., 2022, Subaerial volcaniclastic deposits – influences of initiation mechanisms and transport behaviour on characteristics and distributions: Geological Society, London, Special Publications, v. 520, p. SP520-2021–142, doi:10.1144/SP520-2021-142.

Mariner, R.H., and Surdam, R.C., 1970, Alkalinity and Formation of Zeolites in Saline Alkaline Lakes: Science, v. 170, p. 977–980.

Martin-Bello, L., Arenas, C., and Jones, B., 2019, Lacustrine stromatolites: Useful structures for environmental interpretation – an example from the Miocene Ebro Basin: Sedimentology, v. 66, p. 2098–2133, doi:10.1111/sed.12577.

Martinius, A., Geel, C.R., and Aribas, J., 2002, Lithofacies characterization of fluvial sandstones from outcrop gramma-ray logs (Loranca Basin, Spain): The influence of provenance: Petroleum Geoscience, v. 8, p. 51–62, doi:10.1144/petgeo.8.1.51.

Maxson, J., and Tikoff, B., 1996, Hit-and-run collision model for the Laramide orogeny, western United States: Geology, v. 24, p. 968–972, doi:10.1130/0091-7613(1996)024<0968:HARCMF>2.3.CO;2.

McGowin, E., M., 2015, Spectral gamma ray characterization of the Elko Formation, Nevada - a case study for a small lacustrine basin [Masters]: Colorado State University, https://mountainscholar.org/handle/10217/167118?show=full.

McMillan, M.E., Heller, P.L., and Wing, S.L., 2006, History and causes of post-Laramide relief in the Rocky Mountain orogenic plateau: GSA Bulletin, v. 118, p. 393–405, doi:10.1130/B25712.1.

Meissner, R., and Mooney, W., 1998, Weakness of the lower continental crust: a condition for delamination, uplift, and escape: Tectonophysics, v. 296, p. 47–60, doi:10.1016/S0040-1951(98)00136-X.

Miall, A., 2010, Alluvial Deposits, *in* Facies Models 4, Geological Association of Canada, GEOtext 6, p. 105–138.

Miall, A., 1977, Lithofacies Types and Vertical Profile Models in Braided River Deposits: A Summary:, https://www.semanticscholar.org/paper/Lithofacies-Types-and-Vertical-Profile-Models-in-A-Miall/ae576cfbec2fe5a5b2104fd4fc5274404c12bd22 (accessed February 2023).

Min, K., Mundil, R., Renne, P.R., and Ludwig, K.R., 2000, A test for systematic errors in 40Ar/39Ar geochronology through comparison with U/Pb analysis of a 1.1-Ga rhyolite: Geochimica et Cosmochimica Acta, v. 64, p. 73–98, doi:10.1016/S0016-7037(99)00204-5.

Molzer, P., and Erslev, E., 1995, Oblique convergence during northeast-southwest Laramide compression along the east-west Owl Creek and Casper Mountain Arches, central Wyoming: Aapg Bulletin - AAPG BULL, v. 79, p. 1377–1394.

Moskalewicz, D., Dzieduszyńska, D., Elwirski, Ł., Mroczek, P., Petera-Zganiacz, J., Tylmann, K., and Woźniak, P.P., 2022, Recognition of sedimentary environments using handheld gamma-ray spectrometry in Pleistocene Fennoscandian Ice Sheet glaciogenic basin, northern and central Poland: Marine and Petroleum Geology, v. 140, p. 105679, doi:10.1016/j.marpetgeo.2022.105679.

Nanson, G.C., and Croke, J.C., 1992, A genetic classification of floodplains: Geomorphology, v. 4, p. 459–486, doi:10.1016/0169-555X(92)90039-Q.

Oberhänsli, H., and Allen, P.A., 1987, Stable isotopic signatures of tertiary lake carbonates, Eastern Ebro Basin, Spain: Palaeogeography, Palaeoclimatology, Palaeoecology, v. 60, p. 59–75, doi:10.1016/0031-0182(87)90024-1.

Pekarek, A.H., 1974, The structural geology and volcanic petrology of the Rattlesnake Hills, Wyoming [Ph.D.]: University of Wyoming, 113 p., https://www.proquest.com/docview/302767958/abstract/59568A711382418DPQ/1 (accessed November 2022).

Poupon, A., Clavier, C., Dumanoir, J., Gaymard, R., and Misk, A., 1970, Log Analysis of Sand-Shale SequencesA Systematic Approach: Journal of Petroleum Technology, v. 22, p. 867–881, doi:10.2118/2897-PA.

Prothero, D.R., Scott Anderson, J., Chamberlain, K.R., and Ludtke, J., 2008, Magnetic Stratigraphy and Geochronology of the Barstovian-Clarendonian (Middle to late Miocene) part of the Moonstone Formation, Central Wyoming: Neogene Mammals. New Mexico Meuseum of Natural History and Science Bulletin, v. 44, p. 225–232.

Reijmer, J.J.G., Blok, C.N., El-Husseiny, A., Kleipool, L.M., Hogendorp, Y.C.K., and Alonso-Zarza, A.M., 2022, Petrophysics and sediment variability in a mixed alluvial to lacustrine carbonate system (Miocene, Madrid Basin, Central Spain): The Depositional Record, v. 8, p. 317–339, doi:10.1002/dep2.158.

Renaut, R.W., and Gierlowski-Kordesch, E.H., 2010, Lakes, *in* Facies Models 4, Geological Association of Canada, GEOtext 6, p. 541–575.

Retallack, G., 1988, Field recognition of paleosols: Geological Society of America, v. Special Paper 216, p. 1–19, doi:10.1130/SPE216-p1.

Robinson, P., Gunnell, G.F., Walsh, S.L., Clyde, W.C., Storer, J.E., Stucky, R.K., Froehlich, D.J., Ferrusquia-Villafranca, I., and McKenna, M.C., 2004, Wasatchian Through Duchesnean Biochronology, *in* Woodburne, M.O. ed., Late Cretaceous and Cenozoic Mammals of North America, Columbia University Press, Biostratigraphy and Geochronology, p. 106–155, http://www.jstor.org/stable/10.7312/wood13040.10 (accessed February 2023).

Rowley, D.B., 2007, Stable Isotope-Based Paleoaltimetry: Theory and Validation: Reviews in Mineralogy and Geochemistry, v. 66, p. 23–52, doi:10.2138/rmg.2007.66.2.

Saleeby, J., 2003, Segmentation of the Laramide Slab—evidence from the southern Sierra Nevada region: GSA Bulletin, v. 115, p. 655–668, doi:10.1130/0016-7606(2003)115<0655:SOTLSF>2.0.CO;2.

Sales, J.K., 1984, Collapse of Rocky Mountain basement uplifts: AAPG Bull., v. 68, p. 947–948, doi:10.1306/AD4615ED-16F7-11D7-8645000102C1865D.

Schwartz, T.M., 2021, Compilation of in situ and detrital zircon U-Pb ages for the Jurassic-Paleocene North American Cordillera (28-50 degrees north):, doi:10.5066/P9E5INN9.

Smith, M.E., Carroll, A.R., Jicha, B.R., Cassel, E.J., and Scott, J.J., 2014, Paleogeographic record of Eocene Farallon slab rollback beneath western North America: Geology, v. 42, p. 1039–1042, doi:https://doi.org/10.1130/g36025.1.

Smith, M.E., Carroll, A.R., and Singer, B.S., 2008, Synoptic reconstruction of a major ancient lake system: Eocene Green River Formation, western United States: GSA Bulletin, v. 120, p. 54–84, doi:10.1130/B26073.1.

Smith, M.E., Cassel, E.J., Jicha, B.R., Singer, B.S., and Canada, A.S., 2017, Hinterland drainage closure and lake formation in response to middle Eocene Farallon slab removal, Nevada, U.S.A.: Earth and Planetary Science Letters, v. 479, p. 156–169, doi:10.1016/j.epsl.2017.09.023.

Smith, M.E., Singer, B., and Carroll, A., 2003, 40Ar/39Ar geochronology of the Eocene Green River Formation, Wyoming: GSA Bulletin, v. 115, p. 549–565, doi:10.1130/0016-7606(2003)115<0549:AGOTEG>2.0.CO;2.

Sohn, C., and Sohn, Y.K., 2019, Distinguishing between primary and secondary volcaniclastic deposits: Scientific Reports, v. 9, p. 12425, doi:10.1038/s41598-019-48933-4.

Steidtmann, J.R., and Middleton, L.T., 1991, Fault chronology and uplift history of the southern Wind River Range, Wyoming: Implications for Laramide and post-Laramide deformation in the Rocky Mountain foreland: Geological Society of America Bulletin, v. 103, p. 472–485, doi:10.1130/0016-7606(1991)103<0472:FCAUHO>2.3.CO;2.

Stock, J., and Molnar, P., 1988, Uncertainties and implications of the Late Cretaceous and Tertiary position of North America relative to the Farallon, Kula, and Pacific Plates:, doi:10.1029/TC007I006P01339.

Talbot, M.R., 1990, A review of the palaeohydrological interpretation of carbon and oxygen isotopic ratios in primary lacustrine carbonates: Chemical Geology: Isotope Geoscience section, v. 80, p. 261–279, doi:10.1016/0168-9622(90)90009-2.

Thompson, R., 2015, Post-Laramide, Collapse-Related Fracturing and Production; Wind River Basin, Wyoming: Mountain Geologist, v. 52, doi:10.31582/rmag.mg.52.4.27.

Tikoff, B., Housen, B.A., Maxson, J.A., Nelson, E.M., Trevino, S., and Shipley, T.F., 2023, Hit-and-run model for Cretaceous–Paleogene tectonism along the western margin of Laurentia, *in* Whitmeyer, S.J., Williams, M.L., Kellett, D.A., and Tikoff, B. eds., Laurentia: Turning Points in the Evolution of a Continent, Geological Society of America, v. 220, p. 0, doi:10.1130/2022.1220(32).

Tikoff, B., and Maxson, J., 2001, Lithospheric buckling of the Laramide foreland during Late Cretaceous and Paleogene, western United States: Rocky Mountain Geology, v. 36, p. 13–35, doi:10.2113/gsrocky.36.1.13.

Tourtelot, H.A., 1957, The geology and vertebrate paleontology of upper eocene strata in the northeastern part of the Wind River Basin, Wyoming. Part 1. Geology:, http://repository.si.edu/xmlui/handle/10088/22941 (accessed February 2022).

Trimble, D.E., 1980, Cenozoic Tectonic History of the Great Plains Contrasted with that of the Southern Rocky Mountains: A Synthesis: Mountain Geologist, v. 17, p. 59–69, doi:10.31582/rmag.mg.17.3.59.

Van Houten, F., 1964, Tertiary geology of the Beaver Rim area, Fremont and Natrona Counties, Wyoming: US Geological Survey 1164, doi:10.3133/b1164.

Van Houten, F., 1955, Volcanic-Rich Middle and Upper Eocene Sedimentary Rocks Northwest of Rattlesnake Hills Central Wyoming: Geological Survey Bulletin, v. 274-A.

Weil, A.B., Yonkee, A., and Schultz, M., 2016, Tectonic evolution of a Laramide transverse structural zone: Sweetwater Arch, south central Wyoming: Tectonics, v. 35, p. 1090–1120, doi:10.1002/2016TC004122.

Westerhold, T. et al., 2020, An astronomically dated record of Earth's climate and its predictability over the last 66 million years: Science, v. 369, p. 1383–1387, doi:10.1126/science.aba6853.

Yen, T.-C., 1948, Eocene Fresh-Water Mollusca from Wyoming: Journal of Paleontology, v. 22, p. 634–640.

Zachos, J., Pagani, M., Sloan, L., Thomas, E., and Billups, K., 2001, Trends, Rhythms, and Aberrations in Global Climate 65 Ma to Present: Science, v. 292, p. 686–693, doi:10.1126/science.1059412.

Zamanian, K., Pustovoytov, K., and Kuzyakov, Y., 2016, Pedogenic carbonates: Forms and formation processes: Earth-Science Reviews, v. 157, p. 1–17, doi:10.1016/j.earscirev.2016.03.003.

TABLE 1. LOCATIONS OF STRATIGRAPHIC SECTIONS MEASURED ALONG THE BEAVER RIM

Name	Lattitude (base)	Longitude (base)	Lattitude (top)	Longitude (top)	Total (m)
Sand Draw 1	42.729258	-108.168541	42.721294	-108.170807	105.5
Sand Draw 2	42.722188	-108.169926	42.723641	-108.171322	11.5
Sand Draw 3	42.723087	-108.159806	42.919623	-108.15463	64.75
Gas Hills 1	42.770419	-107.576942	42.769219	-107.576236	32
Gas Hills 2	42.766355	-107.577392	42765712	-107.577517	10
Gas Hills 3	42.801058	-107.489347	42.801597	-107.487748	35
Gas Hills 4	42.766182	-107.607921	42.756029	-107.600071	90
Hwy 287	42.595889	-108.302229	42.599436	-108.289942	51.5

Note. Coordinates are given relative to the WGS 84 datum.

TABLE 2. SUMMARY OF LITHOFACIES CHARACTERISTICS, INTERPRETED ENVIRONMENTS AND LITHOFACIES ASSOCIATIONS

Lithofacies		Avg. grain size	Sorting	Clast/phenocryst composition	Sedimentary structures	Other Characteristics	Interpreted environment	Lithofacies Association
Lf-1	Tuffaceous sandstone	f - m	moderate - very well	biotite, quartz, feldspar	horizontal bedding; parallel and wavy lamination; normal grading; or structureless	ashy matrix; paleosol development; ash-filled root traces; zeolite minerals	Fluvial/floodplain; point bar, crevasse splay, overbank deposits	fluvial
Lf-2	Sandstone	f - c	poor - well	quartz, feldspar, muscovite, dark grains	1-3 cm cross-beds; horizontal bedding; normal grading; or structureless	resistive	fluvial lateral accretion surfaces	fluvial
Lf-3	Tuffaceous mudstone	mud	moderate - well	biotite, quartz	horizontal laminations	heavily weathered at surface; crumbly/flaky; weak paleosol development; brown/gray but weathers white	fluvial/floodplain; overbank deposits	fluvial
Lf-4	Pebble conglomerate	vc - pebble	unsorted - moderate	quartz, feldspar	horizontal bedding; 5-10 cm cross-beds; weak normal grading	matrix supported	fluvial channel; lateral accretion surfaces	fluvial
Lf-5	Carbonate cemented sandstone	vf - m	poor - well	biotite, quartz, feldspar	1-4 cm horizontal bedding; wavy lamination; or structureless	carbonate cement; ashy; zeolite minerals	floodplain soils and/or shallow lacustrine	fluvial/ lacustrine
Lf-6	Sandy limestone	-	-	quartz, dark grains	2-20 cm beds; calcite laminations;	stromatolites 5-30 cm tall; high proportion of siliclastics; light gray	margins of shallow lacustrine	lacustrine
Lf-7	Mudstone	mud	well	-	fine horizontal laminations	interbedded with very fine grained tuff; recessive; highly weathered	shallow lacustrine	lacustrine
Lf-8	Intraclastic reworked tuff	vf -f	poor	biotite, quartz, feldspar, mudballs	subtle 0.5 m cross-beds; normal grading; unstructured	mudball intraclasts incorporated from lower bed; laterally continuous marker bed	fluvial/floodplain; reprocessing of air fall volcanic ash	fluvial/ volcanic
Lf-9	Volcanic pebble conglomerate	pebble	poor	granite, mudball, quartz, andesite, and other minor lithologies	2-15 cm cross-beds; erosive lower bedding surfaces; truncated upper beds; horizontal lamination; normal grading; inverse grading	matrix supported; carbonate cement; rounded clasts	volcanic debris flow/lahar	fluvial/ volcanic

TABLE 3. SINGLE-CRYSTAL SANIDINE AGES OF THE WAGON BED FORMATION: BEAVER RIM AND LYSITE MOUNTAIN AREAS

Sample	Location	Latitude (°N)	Longitude (°W)	Age (Ma)	Analytical Uncertainty (2σ)*	Full Uncertainty (2σ)†	Single sanidine analyses	MSWD
442WB	Lysite Mountain	43.57850	107.61115	50.32	0.08	0.18	20 of 33	1.01
445WB	Lysite Mountain	43.57734	107.61118	50.05	0.15	0.22	1 of 30	-
447WB	Lysite Mountain	43.57882	107.60919	45.15	0.12	0.20	9 of 31	-
450WB	West Beaver Rim	42.72426	108.16924	39.84	0.11	0.16	19 of 33	1.54
452WB	West Beaver Rim	42.72295	108.17010	35.68	0.07	0.13	21 of 30	1.22
451WB	West Beaver Rim	42.72185	108.17251	35.68	0.07	0.13	17 of 35	1.27
W33	East Beaver Rim	42.75603	107.60007	46.92	0.07	0.16	9 of 20	1.33
W34	East Beaver Rim	42.75603	107.60007	46.76	0.07	0.17	4 of 28	0.14

Note. Dates are shown relative to 28.201 Ma Fish Canyon sanidine (Kuiper et al. 2008). MSWD = mean square weighted deviates. Coordinates are given based on the WGS 84 datum.

*Analytical uncertainties have been multiplied by the √MSWD, if greater than 1.

†Full uncertainties incorporate decay constant uncertainty of Min et al. (2000) and standard uncertainty.

TABLE 4. COMPLETE $^{40}AR/^{39}AR$ DATA FOR SINGLE CRYSTAL FUSIONS OF SANIDINE CRYSTALS IN 8 SAMPLES.

Sample: 20WY-442WB						**Identifier: UW160:B51**				**J-value: 0.0106**		**± 0.000016**	**(2σ)**			
	^{40}Ar	$\pm2\sigma_{40}$	^{39}Ar	$\pm2\sigma_{39}$	^{38}Ar	$\pm2\sigma_{38}$	^{37}Ar	$\pm2\sigma_{37}$	^{36}Ar	$\pm2\sigma_{36}$			Age	±2σ	$\%^{40}Ar^*$		Included in
File	(cps)	(cps)	(cps)	(cps)	(cps)	(cps)	(cps)	(cps)	(cps)	(cps)	$^{40}Ar^*/^{39}Ar_K$	±2σ	(Ma)	(Ma)	(%)	K/Ca	wtd. Mean
01A	330899	451	125263	52	1528	43	124	5.7	2.0	1.2	2.6353	0.0047	50.39	0.09	99.80	137.374	X
03A	239848	328	11128	15	140	13	1	4.1	2.2	1.3	21.4844	0.0551	375.25	0.87	99.73	56667.161	
04A	434378	586	84282	39	1043	33	170	7.0	2.9	1.2	5.1411	0.0085	97.05	0.16	99.80	64.547	
05A	365420	504	68231	36	812	30	95	5.2	2.2	1.2	5.3432	0.0094	100.76	0.17	99.81	94.902	
06A	271330	376	102249	45	1239	27	108	5.6	8.1	1.2	2.6285	0.0052	50.26	0.10	99.10	127.931	X
07A	118909	168	44798	29	553	22	54	4.3	3.3	1.2	2.6307	0.0087	50.30	0.16	99.15	111.252	X
08A	279215	383	105738	47	1284	27	106	5.4	2.9	1.1	2.6308	0.0049	50.30	0.09	99.67	135.041	X
09A	260004	358	9445	14	126	12	-2	4.2	1.2	1.3	27.4762	0.0697	467.51	1.05	99.85	-388.727	
10A	241389	330	4742	12	68	9	11	4.9	2.2	1.2	50.7406	0.1657	787.21	2.09	99.73	56.475	
11A	163898	226	61811	36	733	23	55	4.4	2.9	1.1	2.6361	0.0065	50.40	0.12	99.46	151.174	X
12A	332701	451	4699	12	72	9	-3	5.7	1.5	1.2	70.6836	0.2183	1022.83	2.42	99.87	-192.090	
14A	89247	128	32903	26	388	17	28	4.0	8.6	1.5	2.6325	0.0144	50.33	0.27	97.10	157.657	X
15A	189400	259	70641	38	820	35	81	5.0	11.3	1.1	2.6317	0.0062	50.32	0.12	98.20	115.020	X
16A	195032	358	72940	39	882	28	75	5.4	10.3	1.3	2.6301	0.0074	50.29	0.14	98.40	130.224	X
17A	167936	229	63347	35	751	25	70	4.6	4.4	1.0	2.6289	0.0062	50.27	0.12	99.21	120.288	X
18A	165737	231	61890	36	777	29	49	4.0	9.6	1.1	2.6301	0.0065	50.29	0.12	98.26	170.688	X
19A	71461	105	14015	17	184	15	23	3.6	3.0	1.0	5.0323	0.0238	95.04	0.44	98.74	78.982	
20A	176695	242	66862	37	798	29	59	4.4	2.8	1.0	2.6285	0.0059	50.26	0.11	99.51	153.292	X
21A	249245	339	10181	16	132	13	10	4.4	5.3	1.2	24.3170	0.0616	419.44	0.95	99.37	142.088	
22A	221790	301	83939	41	1036	32	67	4.4	1.3	1.0	2.6361	0.0052	50.40	0.10	99.81	169.203	X
23A	160603	221	60502	34	731	25	46	4.0	3.0	1.4	2.6381	0.0078	50.44	0.15	99.43	177.572	X
24A	171836	236	64658	36	785	27	57	4.3	5.7	1.0	2.6295	0.0061	50.28	0.12	98.99	153.810	X
25A	123433	172	45524	30	534	18	66	4.4	11.5	1.1	2.6345	0.0082	50.37	0.15	97.21	90.576	X
26A	163706	226	31183	26	393	15	61	4.9	6.6	1.2	5.1839	0.0143	97.83	0.26	98.79	65.557	

File	^{40}Ar (cps)	$\pm2\sigma_{40}$ (cps)	^{39}Ar (cps)	$\pm2\sigma_{39}$ (cps)	^{38}Ar (cps)	$\pm2\sigma_{38}$ (cps)	^{37}Ar (cps)	$\pm2\sigma_{37}$ (cps)	^{36}Ar (cps)	$\pm2\sigma_{36}$ (cps)	$^{40}Ar^*/^{39}Ar_K$	±2σ	Age (Ma)	±2σ (Ma)	$\%^{40}Ar^*$ (%)	K/Ca	Included in wtd. Mean
27A	243607	331	92015	44	1126	22	110	5.4	5.3	1.0	2.6287	0.0051	50.26	0.10	99.34	110.237	X
28A	145187	201	28640	24	360	18	68	4.5	4.3	1.0	5.0219	0.0133	94.85	0.24	99.11	54.053	
29A	231127	308	9340	15	118	9	0	5.4	1.4	1.1	24.6917	0.0638	425.21	0.98	99.82	-2916.138	
30A	397068	522	148354	56	1776	32	174	7.1	20.2	1.7	2.6342	0.0050	50.37	0.09	98.46	112.456	X
31A	237951	316	90120	43	1104	32	101	5.2	2.6	1.0	2.6303	0.0050	50.29	0.09	99.66	118.047	X
32A	289028	383	53698	31	665	27	160	7.2	4.1	1.0	5.3576	0.0096	101.02	0.18	99.58	42.577	
33A	121852	166	45914	29	556	23	54	4.3	2.4	1.3	2.6365	0.0095	50.41	0.18	99.39	110.678	X
34A	205136	274	77690	39	909	27	73	4.6	2.4	1.0	2.6296	0.0053	50.28	0.10	99.63	141.897	X
35A	161613	217	31341	26	382	26	112	5.7	2.4	1.0	5.1314	0.0123	96.87	0.23	99.55	35.491	
										Weighted mean age (20 of 35):			**50.32**	**0.08**	***0.18*‡**	MSWD:	**1.01**

Sample: 20WY-445WB-A-2 Identifier: UW160:B52 J-value: 0.0106 ± 0.000016 (2σ)

File	^{40}Ar (cps)	$\pm2\sigma_{40}$ (cps)	^{39}Ar (cps)	$\pm2\sigma_{39}$ (cps)	^{38}Ar (cps)	$\pm2\sigma_{38}$ (cps)	^{37}Ar (cps)	$\pm2\sigma_{37}$ (cps)	^{36}Ar (cps)	$\pm2\sigma_{36}$ (cps)	$^{40}Ar^*/^{39}Ar_K$	±2σ	Age (Ma)	±2σ (Ma)	$\%^{40}Ar^*$ (%)	K/Ca	Included in wtd. Mean
01A	228057	311.2	2174	9.01	40	7.32	26	4.83	1.7	1.11	104.6188	0.48135	1364.960	4.43	99.77	10.578	
02A	387100	523.5	18080	19	236	14.9	-2	5.4	9.1	1.15	21.2498	0.0412	371.541	0.65	99.29	-690.181	
03A	264545	360	10820	15.6	135	10.9	3	5.29	1.5	1.08	24.3952	0.05685	420.649	0.88	99.82	565.647	
04A	241980	324.3	7214	12.1	97	8.58	16	4.73	1.7	1.12	33.4612	0.08555	555.238	1.22	99.79	56.401	
05A	319368	426.6	5340	12.5	83	9.26	6	4.39	3.4	1.2	59.5965	0.17417	895.601	2.07	99.69	118.003	
06A	503447	666.5	98568	44.6	1181	22.6	165	6.87	6.1	1.04	5.0867	0.0078	96.044	0.14	99.63	77.034	
07A	366577	479.7	13335	17.2	173	14.3	17	4.37	3.5	1.18	27.3989	0.05692	466.346	0.86	99.72	99.752	
08A	338392	441.9	23491	21.3	300	18.5	15	4.27	5.1	1.11	14.3326	0.02688	258.674	0.45	99.54	218.299	
09A	185796	246	34931	26.5	431	21.5	67	4.95	2.3	1.06	5.2963	0.01216	99.896	0.22	99.62	67.036	
10A	174362	236.9	32459	24.4	392	19.3	65	4.41	22.1	1.15	5.1656	0.01346	97.495	0.25	96.20	63.775	
11A	428567	571.8	20055	20.5	263	16	17	4.39	7.2	1.1	21.2527	0.03944	371.588	0.62	99.50	160.964	
12A	245689	330.3	11028	16.9	154	10.8	2	5.24	4.4	1.14	22.1478	0.05472	385.696	0.86	99.46	858.045	
13A	279896	379.5	54712	33.7	681	23.6	73	4.52	9.0	1.07	5.0642	0.00957	95.630	0.18	99.04	97.699	
14A	161355	221.7	59435	35.4	751	22.9	52	4.28	19.1	1.1	2.6175	0.00685	50.050	0.13	96.46	150.803	X

File	^{40}Ar (cps)	$\pm2\sigma_{40}$ (cps)	^{39}Ar (cps)	$\pm2\sigma_{39}$ (cps)	^{38}Ar (cps)	$\pm2\sigma_{38}$ (cps)	^{37}Ar (cps)	$\pm2\sigma_{37}$ (cps)	^{36}Ar (cps)	$\pm2\sigma_{36}$ (cps)	$^{40}Ar^*/^{39}Ar_K$	±2σ	Age (Ma)	±2σ (Ma)	$\%^{40}Ar^*$ (%)	K/Ca	Included in wtd. Mean
15A	197780	269.9	37558	27.8	437	20.4	90	5.09	2.6	0.97	5.2429	0.01121	98.916	0.21	99.61	52.686	
16A	429843	584.2	82048	41.2	1045	39.3	145	6.43	4.3	0.99	5.2206	0.0084	98.505	0.15	99.69	72.209	
17A	271969	371.1	2862	9.81	48	10.9	24	4.79	1.3	1.12	94.8633	0.36936	1272.981	3.57	99.85	14.545	
18A	326863	445	63047	36.5	759	22.5	110	5.5	5.0	1.01	5.1581	0.00904	97.356	0.17	99.54	72.946	
19A	352921	500.2	4792	10.9	81	7.85	12	3.77	29.1	1.25	71.8050	0.20953	1035.222	2.31	97.54	51.925	
20A	382886	539.7	73914	37.8	915	28.4	158	6.78	8.1	1.06	5.1450	0.00886	97.117	0.16	99.37	59.264	
21A	285839	405.5	5037	11.5	78	7.7	15	4.65	2.1	1.13	56.5964	0.16607	859.596	2.01	99.78	42.657	
23A	335772	471.6	4773	11.8	76	6.82	10	4.26	3.0	1.17	70.1272	0.21247	1016.653	2.36	99.74	58.175	
24A	280528	391.9	52787	32.2	626	20.2	83	4.66	0.6	0.99	5.3082	0.00985	100.114	0.18	99.93	81.172	
26A	401653	534.8	7562	12.8	105	13.7	2	4.4	8.1	1.2	52.7681	0.12322	812.599	1.53	99.40	459.701	
27A	239100	320.3	3880	10.9	51	8.79	9	4.31	3.0	1.17	61.3755	0.21177	916.622	2.49	99.63	55.887	
29A	191930	258.8	35145	27	440	17.2	57	4.24	2.9	0.95	5.4341	0.01169	102.424	0.21	99.55	78.123	
30A	276016	367.1	4669	10.8	64	6.67	-7	5.45	1.4	1.02	59.0056	0.17013	888.566	2.03	99.85	-77.727	
31A	402446	528.2	18121	19.3	236	17.7	10	4.44	6.3	1.17	22.0946	0.04208	384.861	0.66	99.53	251.156	
32A	337636	443.7	21197	20.9	264	11.9	15	4.45	8.5	1.13	15.8015	0.03057	283.231	0.51	99.25	192.129	
36A	88964	126.4	10121	14.6	125	11.2	12	3.63	32.2	1.28	7.8348	0.04125	145.909	0.74	89.17	113.446	
											Weighted mean age (1 of 36): 50.05			**0.15**	***0.22‡***	**MSWD**	-

Sample: 20WY-447WB-A **Identifier: UW160:B53** **J-value: 0.0106** **± 0.000016** **(2σ)**

File	^{40}Ar (cps)	$\pm2\sigma_{40}$ (cps)	^{39}Ar (cps)	$\pm2\sigma_{39}$ (cps)	^{38}Ar (cps)	$\pm2\sigma_{38}$ (cps)	^{37}Ar (cps)	$\pm2\sigma_{37}$ (cps)	^{36}Ar (cps)	$\pm2\sigma_{36}$ (cps)	$^{40}Ar^*/^{39}Ar_K$	±2σ	Age (Ma)	±2σ (Ma)	$\%^{40}Ar^*$ (%)	K/Ca	Included in wtd. Mean
01A	166475	227.2	64864	36.1	798	28.4	161	6.57	33.3	1.29	2.41224	0.00702	46.175	0.13	94.03	50.330	
02A	3644	23.07	368	5.79	25	7.43	2	3.61	5.6	1.03	5.33588	0.84197	100.622	15.45	53.90	18.644	
03A	3279	22.69	152	5.51	15	5.86	4	3.58	7.6	1.01	6.75252	2.00623	126.433	36.30	31.27	5.063	
05A	8479	26	776	6.47	20	7.29	44	3.82	18.1	1.1	3.96980	0.42641	75.383	7.93	36.35	2.150	
06A	223057	303.6	86262	41.9	1032	31.3	216	8.03	65.6	1.71	2.35774	0.007	45.145	0.13	91.22	49.829	X
07A	155835	215.2	57612	33.4	707	23.4	178	7.3	32.1	1.26	2.53737	0.00769	48.539	0.15	93.85	40.303	
08A	82416	117.6	26957	22.8	337	17.3	68	4.53	58.7	1.58	2.40623	0.01822	46.062	0.34	78.74	49.221	

File	^{40}Ar (cps)	±2σ$_{40}$ (cps)	^{39}Ar (cps)	±2σ$_{39}$ (cps)	^{38}Ar (cps)	±2σ$_{38}$ (cps)	^{37}Ar (cps)	±2σ$_{37}$ (cps)	^{36}Ar (cps)	±2σ$_{36}$ (cps)	^{40}Ar*/^{39}Ar$_K$	±2σ	Age (Ma)	±2σ (Ma)	%^{40}Ar* (%)	K/Ca	Included in wtd. Mean
09A	2951	21.83	109	5.43	11	6.2	20	3.82	8.2	0.98	4.72512	2.6926	89.381	49.71	17.53	0.660	
10A	184409	244.9	61214	34.9	772	23.9	318	11.9	113	2.41	2.46022	0.01254	47.082	0.24	81.70	23.682	
12A	25328	44.14	8242	13.8	104	8.63	2236	77.7	18.6	1.09	2.47563	0.04005	47.373	0.76	80.55	0.448	
13A	10727	27.05	133	5.3	18	6.06	3	3.62	20.7	1.08	34.16630	2.79677	565.303	39.81	42.38	5.585	
14A	3340	21.9	109	5.25	12	5.4	7	3.87	9.1	0.99	5.78939	2.74697	108.925	50.17	18.87	1.804	
16A	7776	24.96	433	5.82	22	5.79	24	3.99	18.1	1.1	5.50895	0.76518	103.795	14.02	30.72	2.192	
17A	3723	21.97	228	5.45	22	5.24	2	3.79	9.3	1	4.21182	1.322	79.880	24.53	25.78	17.519	
18A	9524	25.82	486	5.77	21	6.5	9	3.81	20.7	1.13	6.90524	0.70198	129.194	12.68	35.25	6.490	
19A	5794	23.51	179	5.41	12	5.76	10	3.68	15.0	1.03	7.37403	1.73672	137.642	31.23	22.82	2.186	
20A	6596	24.6	83	5.3	11	6.95	-4	3.72	20.3	1.08	6.46884	3.8971	121.293	70.70	8.17	-2.632	
21A	144052	192.7	54126	32.6	656	27	144	6.33	27.8	1.18	2.50675	0.0076	47.961	0.14	94.23	46.635	
22A	9493	26.17	276	5.43	21	8.95	2	3.61	25.9	1.14	6.40881	1.24304	120.204	22.57	18.65	14.891	
23A	261616	352.7	103064	46.4	1231	41.9	92	5.03	8.9	1	2.51097	0.00463	48.041	0.09	98.96	145.760	
24A	5849	23.59	1269	6.92	29	6.42	3	3.7	7.8	1	2.77240	0.23743	52.971	4.47	60.17	53.059	
26A	259328	338.4	95717	43.2	1159	28.1	376	13.5	63.4	1.63	2.51078	0.00632	48.037	0.12	92.71	31.188	
27A	183056	240	69633	37	851	25.2	184	7.46	34.3	1.29	2.48084	0.00666	47.472	0.13	94.41	46.670	
28A	199020	258.2	68801	36.1	844	32.3	162	6.82	92.6	2	2.48961	0.00956	47.637	0.18	86.10	52.658	
29A	33349	52.29	11741	15.3	143	16.9	35	3.83	13.0	1.04	2.50988	0.027	48.020	0.51	88.41	41.331	
30A	141812	186.7	53488	32.5	639	21.3	146	6.25	36.2	1.32	2.44822	0.00828	46.855	0.16	92.38	45.190	
31A	121803	166.1	45712	31.1	589	19.1	190	7.63	34.9	1.23	2.43621	0.00898	46.629	0.17	91.47	29.395	
32A	203146	271.1	74583	37.4	923	33.1	202	7.97	86.9	1.95	2.37469	0.0087	45.465	0.16	87.22	45.462	
34A	126534	175.6	49158	31.8	610	26.8	138	6.07	31.9	1.29	2.37923	0.00878	45.551	0.17	92.47	43.893	
35A	9530	26.59	1242	7.07	30	6.73	19	3.67	16.6	1.11	3.67717	0.26904	69.931	5.02	47.94	7.943	
36A	150441	207.5	55596	32.9	683	29.1	152	6.42	40.4	1.37	2.48796	0.00839	47.606	0.16	91.99	45.059	
											Weighted mean age (1 of 36):		**45.15**	**0.12**	***0.20‡***	**MSWD**	-

Sample: 20WY-450WB-B **Identifier: UW160:B55** **J-value: 0.0106** **± 0.000016** **(2σ)**

	^{40}Ar	±2σ$_{40}$	^{39}Ar	±2σ$_{39}$	^{38}Ar	±2σ$_{38}$	^{37}Ar	±2σ$_{37}$	^{36}Ar	±2σ$_{36}$			Age	±2σ	%^{40}Ar*		Included in

File	(cps)	(cps)	(cps)	(cps)	(cps)	(cps)	(cps)	(cps)	(cps)	(cps)	$^{40}Ar^*/^{39}Ar_K$	±2σ	(Ma)	(Ma)	(%)	K/Ca	wtd. Mean
01A	105876	142.8	50801	31.5	631	29.4	49	4.49	1.0	1.11	2.076667	0.0072	99.69	39.82	0.137	131.687	X
02A	44752	66.77	5982	11.4	111	12.2	102	5.01	127	2.52	1.130418	0.12705	15.12	21.78	2.434	7.008	
03A	102785	144.1	49339	31.4	609	18.2	47	4.03	1.5	0.89	2.073034	0.00629	99.56	39.75	0.119	134.694	X
04A	27596	46.46	3710	9.54	66	7.46	107	5.47	61.8	1.65	2.469307	0.13358	33.21	47.25	2.524	4.134	
05A	27389	45.39	1603	7.07	32	4.99	39	4.02	12.8	0.99	14.703651	0.19679	86.08	264.91	3.301	4.862	
06A	94891	172.6	45062	29.7	540	21.6	39	4.24	5.0	0.97	2.071135	0.00758	98.40	39.72	0.144	149.180	X
07A	337132	432.1	3925	9.6	54	7.16	3	3.6	-2.8	0.83	86.078750	0.24587	100.25	1186.00	2.493	173.968	
08A	79090	108	37433	26.9	463	23.6	34	3.86	3.1	0.87	2.086348	0.00766	98.79	40.00	0.145	139.516	X
09A	6335	22.98	2625	8.38	51	7.26	68	4.32	9.6	0.91	1.325601	0.1044	54.95	25.52	1.996	4.590	
10A	7501	23.6	3260	9.02	48	5.56	63	4.31	13.1	0.97	1.106116	0.0896	48.09	21.32	1.717	6.208	
11A	40927	61.62	19430	20	246	20.3	26	3.7	1.5	0.89	2.082286	0.01415	98.90	39.93	0.268	93.466	X
12A	77388	108.3	37082	26.9	450	21.1	39	3.86	1.4	0.9	2.074257	0.00799	99.44	39.78	0.151	119.273	X
13A	79151	110.7	5117	10.3	110	11.2	140	6	244	4.3	1.231315	0.25363	7.96	23.72	4.853	4.357	
14A	104245	143.1	8402	13.2	165	9.04	167	6.7	308	5.3	1.470361	0.19047	11.86	28.28	3.636	5.963	
15A	114101	156.6	6515	11.8	158	11.5	181	7	348	5.78	1.589042	0.26793	9.08	30.55	5.108	4.266	
16A	349456	466.2	3769	9.38	53	6.59	-4	5.35	-2.8	0.87	92.888120	0.27105	100.24	1253.78	2.649	-103.912	
17A	87771	122.9	41725	28.4	513	24.5	46	4.03	2.3	0.91	2.085783	0.00726	99.20	39.99	0.138	114.584	X
18A	123967	236.5	59310	29.7	719	26.5	68	4.69	1.8	0.91	2.079566	0.00616	99.54	39.88	0.117	104.373	X
19A	59383	83.88	28369	21.4	340	19.8	40	3.66	1.2	0.85	2.078808	0.00954	99.36	39.86	0.181	83.742	X
20A	115167	219.9	55248	31.4	664	29	43	3.82	1.8	0.89	2.073092	0.00635	99.50	39.75	0.121	156.429	X
21A	346955	454.1	4775	9.12	70	10.3	2	3.51	-2.4	0.87	72.769197	0.17696	100.21	1045.81	1.937	270.466	
22A	448354	598.4	4101	11.6	62	18.5	14	4.1	-0.5	0.99	109.32409	0.34842	100.04	1407.72	3.130	33.033	
23A	33839	52.77	16038	17.5	256	21.5	16	3.5	1.1	0.94	2.088163	0.0179	99.01	40.04	0.339	120.616	X
24A	481111	638.1	6165	12.4	87	14.6	17	3.76	-2.9	0.95	78.148277	0.19346	100.18	1103.77	2.052	40.944	
25A	83531	116.8	39739	26.7	485	19.9	43	3.88	2.2	0.9	2.084071	0.00749	99.19	39.96	0.142	110.160	X
27A	24315	43.06	11422	13.9	153	13.4	79	4.63	6.1	0.95	1.969167	0.02523	92.55	37.78	0.479	16.649	
28A	139324	188.8	66768	33.5	823	28.1	86	4.59	2.5	0.9	2.074310	0.00502	99.45	39.78	0.095	92.246	X
29A	38235	58.15	18079	18	223	12.3	23	3.57	1.5	0.91	2.088508	0.0155	98.80	40.05	0.294	92.892	X

File	^{40}Ar (cps)	±2σ$_{40}$ (cps)	^{39}Ar (cps)	±2σ$_{39}$ (cps)	^{38}Ar (cps)	±2σ$_{38}$ (cps)	^{37}Ar (cps)	±2σ$_{37}$ (cps)	^{36}Ar (cps)	±2σ$_{36}$ (cps)	^{40}Ar*/^{39}Ar$_K$	±2σ	Age (Ma)	±2σ (Ma)	%^{40}Ar* (%)	K/Ca	Included in wtd. Mean
30A	46923	70.87	22381	19.5	280	13.5	33	3.82	1.0	0.92	2.082213	0.01276	99.36	39.93	0.242	79.945	X
31A	71222	99.83	33997	25.3	412	14.8	28	3.71	1.9	0.91	2.076402	0.00862	99.16	39.82	0.163	145.494	X
32A	49526	72.56	23655	20.3	281	17.5	20	3.41	1.2	0.93	2.077666	0.01226	99.28	39.84	0.233	147.273	X
33A	69406	97.69	32575	23.4	386	18.3	28	3.55	5.7	0.96	2.076451	0.00939	97.50	39.82	0.178	140.468	X
34A	23486	40.53	11129	14.2	126	13.6	17	3.43	1.0	0.9	2.081163	0.02459	98.66	39.91	0.466	75.393	X
											Weighted mean age (20 of 34): 39.84			**0.07**	***0.16‡***	**MSWD**	**1.54**

Sample: 20WY-451WB **Identifier: UW160:B56** **J-value: 0.0106** **± 0.000016** **(2σ)**

File	^{40}Ar (cps)	±2σ$_{40}$ (cps)	^{39}Ar (cps)	±2σ$_{39}$ (cps)	^{38}Ar (cps)	±2σ$_{38}$ (cps)	^{37}Ar (cps)	±2σ$_{37}$ (cps)	^{36}Ar (cps)	±2σ$_{36}$ (cps)	^{40}Ar*/^{39}Ar$_K$	±2σ	Age (Ma)	±2σ (Ma)	%^{40}Ar* (%)	K/Ca	Included in wtd. Mean
01A	134694	179.7	71997	37.4	890	28.9	69	4.2	2.1	0.91	1.8609186	0.00463	35.724	0.09	99.52	125.125	X
02A	101296	137.3	54082	31.6	650	14.4	93	4.71	2.4	1.21	1.8588508	0.00721	35.685	0.14	99.29	68.289	X
03A	133115	183.3	71179	34.5	854	32.1	60	4.26	1.7	0.9	1.8615474	0.00467	35.736	0.09	99.59	145.201	X
04A	179078	243.1	95860	42.5	1154	21.5	100	5.02	2.2	0.94	1.8599721	0.00395	35.706	0.08	99.61	114.067	X
05A	217025	293.1	113371	47.1	1332	22.9	123	5.69	20.0	1.11	1.8601797	0.00398	35.710	0.08	97.22	109.830	X
06A	68722	101.3	36588	24.6	425	15	30	3.8	1.7	0.92	1.8629052	0.00808	35.762	0.15	99.23	146.404	X
08A	126499	180.2	67726	35.3	831	22.7	57	4.01	1.7	0.91	1.8588963	0.00491	35.686	0.09	99.57	144.991	X
10A	122046	169.9	65417	34.2	810	21	67	4.24	2.5	0.92	1.8531559	0.00504	35.577	0.10	99.38	116.519	X
11A	111022	156.4	59442	32.1	703	24	51	3.94	1.7	0.92	1.8579747	0.0054	35.668	0.10	99.53	139.957	X
12A	109679	149.6	58704	32.5	700	16.6	49	4.05	2.0	0.91	1.8569401	0.00538	35.649	0.10	99.44	144.751	X
13A	144116	194	77137	38.4	927	35.5	71	4.25	2.1	0.93	1.8586479	0.0045	35.681	0.09	99.53	131.181	X
14A	140545	189.3	75268	38.4	905	20.2	70	4.22	1.9	0.92	1.8584606	0.00452	35.678	0.09	99.58	129.051	X
15A	135404	181.4	72538	36.4	874	25.2	84	4.55	2.6	0.92	1.8545268	0.00464	35.603	0.09	99.40	102.351	X
16A	124781	168.2	66342	35	784	25.7	76	4.35	5.3	0.97	1.8556880	0.00515	35.625	0.10	98.71	103.884	X
17A	96438	132.1	51635	30.9	617	22.6	44	3.79	2.1	0.9	1.8540907	0.00591	35.594	0.11	99.32	141.368	X
18A	141723	189.1	75907	36.3	920	29.4	77	4.28	2.6	0.93	1.8556049	0.00452	35.623	0.09	99.43	117.220	X
19A	109087	147.7	57851	32.6	719	21.7	72	4.43	3.0	1.24	1.8690874	0.00699	35.880	0.13	99.17	94.034	
20A	121589	163.6	64946	33.2	785	31.9	74	4.38	1.9	0.93	1.8621123	0.00505	35.747	0.10	99.51	104.003	X

File	^{40}Ar (cps)	$\pm2\sigma_{40}$ (cps)	^{39}Ar (cps)	$\pm2\sigma_{39}$ (cps)	^{38}Ar (cps)	$\pm2\sigma_{38}$ (cps)	^{37}Ar (cps)	$\pm2\sigma_{37}$ (cps)	^{36}Ar (cps)	$\pm2\sigma_{36}$ (cps)	$^{40}Ar^*/^{39}Ar_K$	±2σ	Age (Ma)	±2σ (Ma)	$\%^{40}Ar^*$ (%)	K/Ca	Included in wtd. Mean
21A	84996	117.6	45261	28.6	555	18	56	4.15	2.9	1.26	1.8574884	0.00879	35.659	0.17	98.96	94.325	X
22A	121588	165.1	63975	33.8	796	19.5	54	4.19	8.1	0.97	1.8615048	0.00531	35.735	0.10	97.99	141.823	X
23A	71806	101.1	38278	27.1	493	14.3	35	3.89	1.1	0.92	1.8660889	0.00775	35.823	0.15	99.52	131.073	
24A	86487	122.1	46099	28.6	553	16.4	44	4.1	1.4	0.9	1.8658847	0.00649	35.819	0.12	99.50	123.684	
26A	112481	156.5	59709	32.2	709	20.6	53	4.01	1.3	0.89	1.8757482	0.00527	36.006	0.10	99.62	134.935	
27A	103763	144.4	55229	31.5	672	18.3	51	4.12	1.8	1.2	1.8675776	0.00708	35.851	0.13	99.45	127.936	
28A	130780	180.1	68918	34.4	804	29.2	75	4.56	6.9	0.94	1.8662447	0.00494	35.825	0.09	98.39	108.060	
30A	120677	165.2	64332	34.1	777	37	57	4.15	1.7	1.2	1.8664150	0.00621	35.829	0.12	99.54	135.078	
31A	74978	106	39838	26.4	476	19.3	29	3.68	2.3	1.22	1.8636224	0.00961	35.776	0.18	99.07	164.201	X
32A	48538	71.75	11135	14.5	154	11.9	381	13.6	59.8	1.59	2.7649702	0.04348	52.831	0.82	63.46	3.262	
33A	91574	125.9	48338	28.9	592	16.9	30	3.64	1.6	0.9	1.8831030	0.00626	36.146	0.12	99.45	199.210	
35A	44283	67.78	23664	20.4	286	14.4	73	4.39	1.6	0.88	1.8510494	0.01163	35.537	0.22	98.96	36.571	X
											Weighted mean age (21 of 35):		**35.68**	**0.06**	***0.13‡***	**MSWD:**	**1.22**

Sample: 20WY-452WB-B **Identifier: UW160:B57** **J-value: 0.0106** **± 0.000016** **(2σ)**

File	^{40}Ar (cps)	$\pm2\sigma_{40}$ (cps)	^{39}Ar (cps)	$\pm2\sigma_{39}$ (cps)	^{38}Ar (cps)	$\pm2\sigma_{38}$ (cps)	^{37}Ar (cps)	$\pm2\sigma_{37}$ (cps)	^{36}Ar (cps)	$\pm2\sigma_{36}$ (cps)	$^{40}Ar^*/^{39}Ar_K$	±2σ	Age (Ma)	±2σ (Ma)	$\%^{40}Ar^*$ (%)	K/Ca	Included in wtd. Mean
01A	165784	313.2	88844	40.8	1060	29.8	108	6.19	2.8	0.89	1.8554425	0.00471	35.620	0.09	99.48	96.102	X
02A	260708	339.1	139921	49.7	1689	41	140	6.03	3.0	0.94	1.8554964	0.00322	35.621	0.06	99.63	118.241	X
03A	240272	306.8	128603	50.8	1550	36.2	209	8.11	2.9	1.23	1.8604459	0.0038	35.715	0.07	99.63	70.984	X
04A	166740	228.3	89488	39.8	1076	27.9	134	5.93	0.7	0.91	1.8596733	0.00406	35.701	0.08	99.86	77.365	X
05A	217374	294.8	116449	44.3	1443	34	162	6.73	1.9	0.93	1.8607100	0.00355	35.720	0.07	99.73	83.386	X
06A	126246	175.2	67519	34.8	822	30.2	101	5.03	2.9	0.92	1.8558290	0.00493	35.627	0.09	99.30	76.914	X
07A	12955	31.13	6059	11.2	82	8.33	123	5.54	1.4	0.88	2.0760571	0.04384	39.810	0.83	97.14	5.491	
08A	108154	152.9	57997	32.6	689	19.6	81	4.45	1.5	0.92	1.8561183	0.00551	35.633	0.10	99.58	82.714	X
09A	25032	43.81	12999	15.1	188	8.58	235	8.8	2.2	0.91	1.8787397	0.02118	36.063	0.40	97.61	6.155	
10A	140273	204.4	75034	36.6	922	34	82	4.56	1.4	1.21	1.8625854	0.00562	35.756	0.11	99.68	107.324	X
11A	26668	45.11	11633	15.1	160	13.1	216	8.16	5.5	0.95	2.1558765	0.02472	41.323	0.47	94.08	5.974	

File	^{40}Ar (cps)	$\pm2\sigma_{40}$ (cps)	^{39}Ar (cps)	$\pm2\sigma_{39}$ (cps)	^{38}Ar (cps)	$\pm2\sigma_{38}$ (cps)	^{37}Ar (cps)	$\pm2\sigma_{37}$ (cps)	^{36}Ar (cps)	$\pm2\sigma_{36}$ (cps)	$^{40}Ar^*/^{39}Ar_K$	±2σ	Age (Ma)	±2σ (Ma)	$\%^{40}Ar^*$ (%)	K/Ca	Included in wtd. Mean
12A	27504	46.97	14007	16.3	197	9.21	236	8.73	2.0	0.91	1.9249763	0.01991	36.942	0.38	98.08	6.579	
13A	33029	53.72	17192	18.4	234	17.3	280	10	4.9	0.95	1.8393389	0.01687	35.314	0.32	95.78	6.818	
14A	33538	54.05	15875	17.3	222	11.8	286	10.2	2.8	0.93	2.0631336	0.01799	39.565	0.34	97.70	6.148	
15A	21121	39.39	10631	15.1	154	13.8	191	7.37	2.9	0.91	1.9083269	0.02594	36.625	0.49	96.10	6.164	
16A	240088	313.2	128652	49.7	1556	36.8	176	7.01	2.8	0.94	1.8585350	0.00335	35.679	0.06	99.64	84.370	X
17A	44024	65.61	22029	19.8	289	18.7	399	13.8	3.0	0.93	1.9619798	0.0131	37.645	0.25	98.22	6.105	
18A	26922	45.03	12576	15.2	174	9.76	259	9.48	2.8	0.93	2.0784360	0.0226	39.855	0.43	97.13	5.366	
19A	170080	228	91158	40	1110	28.7	100	4.96	2.5	0.94	1.8561233	0.00406	35.633	0.08	99.53	106.151	X
20A	114517	156.5	8635	12	176	13.2	183	7.17	322	5.74	2.1500955	0.20058	41.214	3.80	16.22	5.223	
21A	169339	224.3	90070	39.9	1085	29.8	109	5.17	4.8	1.3	1.8630301	0.00505	35.764	0.10	99.14	95.161	X
22A	223859	302.5	118899	46.5	1431	38.5	132	5.77	8.4	1.32	1.8604687	0.00424	35.716	0.08	98.86	104.657	X
23A	19151	36.83	9535	12.9	138	7.44	170	6.87	2.0	0.93	1.9504163	0.02954	37.425	0.56	97.15	6.178	
24A	20772	38.48	9919	14	142	12.1	192	7.45	1.3	0.94	2.0597877	0.02873	39.501	0.55	98.40	5.700	
25A	182803	244.2	96248	40.5	1161	32.2	67	4.21	2.1	0.94	1.8912388	0.00395	36.301	0.08	99.62	172.252	
26A	149316	201	79877	38.8	997	25	79	4.56	2.4	0.94	1.8591473	0.00443	35.691	0.08	99.50	118.050	X
27A	13869	30.42	4027	8.69	68	6.93	63	4.26	21.1	1.1	1.8860878	0.08235	36.203	1.57	54.78	7.030	
28A	178075	243.2	95331	42	1136	21.9	169	6.74	1.8	0.95	1.8611238	0.00401	35.728	0.08	99.68	64.050	X
29A	142724	196.1	76454	37.2	921	27.6	90	4.7	1.3	1.21	1.8606248	0.00547	35.719	0.10	99.72	97.517	X
30A	35353	377.6	12098	60.8	1798	44.6	326	11.4	42.0	2.22	1.8986967	0.06385	36.442	1.21	65.00	4.085	
31A	15907	33.83	7423	12.4	102	7.62	157	6.53	1.5	0.94	2.0882117	0.03839	40.040	0.73	97.48	5.210	
32A	139791	185.9	74996	37.1	898	23.6	145	6.28	1.3	0.97	1.8577191	0.00469	35.663	0.09	99.71	58.396	X
33A	42253	62.61	19993	20.6	270	16.6	395	14.2	1.9	0.97	2.0892408	0.01494	40.060	0.28	98.90	5.552	
34A	21918	40.91	10146	13.7	157	12	197	7.68	1.7	0.96	2.1156570	0.02876	40.561	0.55	97.98	5.649	
35A	165281	227.4	88715	39	1071	29.6	117	5.47	1.4	0.97	1.8572089	0.00423	35.654	0.08	99.74	86.495	X
											Weighted mean age (17 of 35):		**35.68**	**0.06**	***0.13‡***	**MSWD:**	**1.27**

Sample: W33 **Identifier: UW164:D76** **J-value: 0.0138** **± 0.000014** **(2σ)**

	^{40}Ar	$\pm2\sigma_{40}$	^{39}Ar	$\pm2\sigma_{39}$	^{38}Ar	$\pm2\sigma_{38}$	^{37}Ar	$\pm2\sigma_{37}$	^{36}Ar	$\pm2\sigma_{36}$			Age	±2σ	$\%^{40}Ar^*$		Included in

File	(cps)	(cps)	(cps)	(cps)	(cps)	(cps)	(cps)	(cps)	(cps)	(cps)	$^{40}Ar^*/^{39}Ar_K$	±2σ	(Ma)	(Ma)	(%)	K/Ca	wtd. Mean
08A	166274	339	87714	70.9	1014	30.6	71	5.43	13.4	0.8	1.8809	0.00538	46.78	0.13211	99.29	64.84	X
10A	335512	514	168863	62.4	1989	48.8	153	6.4	13.4	0.8	1.8993	0.0041	47.24	0.10063	95.66	57.41	
11A	213538	330	112729	50.9	1357	39.9	91	5.24	13.4	0.8	1.8861	0.00403	46.91	0.09887	99.64	64.74	X
13A	186689	288	98230	46.3	1197	34.2	74	5.02	13.4	0.8	1.8876	0.00431	46.95	0.10595	99.39	69.28	X
17A	289293	436	151813	60.4	1831	28.4	124	5.93	13.6	0.8	1.8911	0.00357	47.03	0.08768	99.31	64.15	
24A	335064	494	176292	65.3	2116	58	177	6.79	13.8	0.8	1.8884	0.00341	46.97	0.08365	99.43	51.49	X
25A	138616	213	72786	40.6	875	36.6	65	4.96	13.7	0.8	1.8880	0.00526	46.96	0.12926	99.21	57.97	X
32A	60775	96	30743	26.1	369	16.1	26	4.72	13.7	0.8	1.9110	0.01025	47.52	0.25163	96.74	61.86	
34A	137049	212	71048	40.8	866	24	58	5.11	14.2	0.8	1.8954	0.00543	47.14	0.13333	98.33	63.62	
37A	157918	344	83281	44.1	976	33.1	65	5.24	14.6	1.2	1.8841	0.00607	46.86	0.149	99.44	66.86	X
38A	265349	573	140628	59.4	1665	34.2	97	5.46	14.6	1.2	1.8824	0.00489	46.82	0.12001	99.83	75.37	X
39A	291166	424	130050	53.9	1586	30.5	128	5.56	12.0	0.7	1.9037	0.00692	47.34	0.17	85.09	42.13	
41A	62883	99	5250	11.3	99	11.4	398	11.2	12.9	0.7	6.9455	0.11131	167.12	2.55969	57.71	0.53	
42A	203158	299	104654	51.7	1244	33.1	59	4.69	12.7	0.8	1.9072	0.0042	47.43	0.1032	98.32	74.54	
43A	235129	346	116725	50.7	1412	44.5	75	4.71	12.7	0.8	1.9039	0.00469	47.35	0.11515	94.59	64.84	
44A	129319	192	66343	37.5	757	32.8	39	4.49	12.1	0.8	1.8939	0.00571	47.10	0.14014	97.24	71.15	
47A	309825	452	21019	20.4	382	13.8	510	14.5	11.7	0.8	9.2504	0.08443	219.37	1.88677	62.69	1.66	
48A	304590	444	160566	63.1	1937	34.4	111	5.55	11.7	0.8	1.8881	0.00335	46.96	0.08231	99.61	60.00	X
49A	146836	218	12043	16.6	233	19.8	82	4.94	11.7	0.8	3.0352	0.1358	74.92	3.28406	24.90	5.91	
50A	174543	271	90039	43.1	1062	35.7	69	4.72	11.4	0.8	1.8857	0.00466	46.90	0.11433	97.35	53.70	X
											Weighted mean age (9 of 20):		**46.92**	**0.06**	***0.16‡***	**MSWD:**	**1.33**

Sample: W33 **Identifier: UW164:D77** **J-value: 0.0138** **± 0.000014** **(2σ)**

File	^{40}Ar (cps)	$\pm2\sigma_{40}$ (cps)	^{39}Ar (cps)	$\pm2\sigma_{39}$ (cps)	^{38}Ar (cps)	$\pm2\sigma_{38}$ (cps)	^{37}Ar (cps)	$\pm2\sigma_{37}$ (cps)	^{36}Ar (cps)	$\pm2\sigma_{36}$ (cps)	$^{40}Ar^*/^{39}Ar_K$	±2σ	Age (Ma)	±2σ (Ma)	$\%^{40}Ar^*$ (%)	K/Ca	Included in wtd. Mean
01A	222082	13.3	87540	48	1060	0.83	58	4.93	161	2.82	1.9855	0.01049	49.35	0.25723	78.32	74.96	
02A	161748	13.26	4871	10.8	116	0.71	121	5.55	263	4.01	17.1306	0.25625	387.51	5.22401	51.55	1.91	
03A	261067	13.22	12151	16.5	279	0.7	141	5.84	534	7.53	8.3694	0.19011	199.57	4.29475	38.96	4.09	
08A	535540	12.87	6481	11.5	70	0.64	9	4.46	1.8	0.96	82.4864	0.19466	1388.56	2.29651	99.90	33.89	

File	^{40}Ar (cps)	±2σ$_{40}$ (cps)	^{39}Ar (cps)	±2σ$_{39}$ (cps)	^{38}Ar (cps)	±2σ$_{38}$ (cps)	^{37}Ar (cps)	±2σ$_{37}$ (cps)	^{36}Ar (cps)	±2σ$_{36}$ (cps)	^{40}Ar*/^{39}Ar$_K$	±2σ	Age (Ma)	±2σ (Ma)	%^{40}Ar* (%)	K/Ca	Included in wtd. Mean
09A	90563	12.87	8534	14.5	130	0.64	607	17.2	116	2.15	6.6415	0.07848	160.12	1.81151	62.35	0.66	
10A	9531	12.87	1070	6.37	14	0.64	15	4.4	15.4	1.04	4.6306	0.2939	113.10	6.96096	51.96	3.29	
11A	165764	13.29	13374	17.6	238	0.64	136	5.91	280	4.11	6.1491	0.09493	148.71	2.2051	49.62	4.66	
12A	450098	13.29	14411	17.8	446	0.64	157	6.27	1251	15.7	5.3214	0.33324	129.39	7.82278	17.04	4.35	
13A	258957	13.29	11156	16.3	241	0.64	190	7.04	394	5.49	12.6931	0.15368	294.73	3.29602	54.67	2.78	
14A	192732	13.3	82282	44.2	988	0.68	67	4.76	110	2.13	1.9405	0.00864	48.25	0.21212	82.91	60.37	
15A	285478	13.3	3165	9.35	42	0.68	1	4.32	5.2	0.99	89.6359	0.31328	1471.02	3.53321	99.46	203.49	
18A	61809	12.92	20470	21.4	282	0.71	178	6.93	13.2	1.04	2.8316	0.0162	69.98	0.3929	93.80	5.46	
19A	225275	16.5	5509	11.8	102	1.01	50	5.68	134	2.46	33.6311	0.16457	696.32	2.83407	82.26	5.21	
20A	128365	12.92	6685	12.9	138	0.71	114	5.66	210	3.27	9.8332	0.1517	232.35	3.36628	51.19	2.76	
21A	350052	12.92	16116	19.9	312	0.71	192	7.11	519	7.02	12.1099	0.13645	282.18	2.94653	55.75	3.97	
22A	181741	12.92	11744	16.3	232	0.71	167	6.53	369	5.21	6.1003	0.13622	147.58	3.16615	39.42	3.33	
23A	168289	12.72	5362	11.3	96	0.7	51	4.63	106	2.08	25.4771	0.13707	550.22	2.55662	81.20	4.94	
24A	112987	12.72	5457	11.2	115	0.7	65	4.97	239	3.69	7.6510	0.20664	183.27	4.70999	36.95	3.96	
26A	137875	12.6	4522	9.76	93	0.64	185	6.88	163	2.93	19.7727	0.20524	440.60	4.06444	64.73	1.15	
28A	357285	12.6	188927	69.9	2244	0.64	121	5.66	6.3	1.03	1.8794	0.00341	46.75	0.08382	99.46	76.46	X
29A	234876	12.6	7310	12.7	210	0.64	68	4.77	571	8.48	8.8273	0.35362	209.89	7.94378	27.48	5.07	
34A	311299	13.39	164422	62.7	1994	0.65	127	5.79	6.5	1.02	1.8800	0.00338	46.76	0.08312	99.37	62.83	X
35A	308667	13.39	8635	14.5	290	0.65	96	5.27	886	12.4	5.1257	0.43671	124.79	10.2775	14.34	4.22	
37A	74756	13.39	4862	10.7	99	0.65	39	4.66	159	2.82	5.6117	0.17628	136.19	4.12266	36.51	5.92	
43A	243569	12.06	11465	16.5	302	0.66	87	4.87	752	10.4	1.6698	0.27466	41.59	6.76433	7.86	5.30	
44A	238653	12.06	126044	53.7	1515	0.66	82	4.88	5.0	0.92	1.8798	0.00363	46.76	0.08908	99.36	63.61	X
46A	283162	11.16	149692	60.1	1806	0.64	86	4.8	4.5	0.92	1.8809	0.0035	46.79	0.08585	99.52	71.93	X
49A	270420	11.15	132890	55.7	1610	0.72	101	5.14	51.1	1.39	1.9184	0.00451	47.71	0.11065	94.35	54.19	
											Weighted mean age (4 of 28):		**46.76**	**0.07**	***0.17‡***	**MSWD:**	**0.14**

Note. Ages calculated relative to 28.201 Ma Fish Canyon sanidine standard (Kuiper et al., 2008). Errors quoted for individual analyses include analytical error only, without interfering reactions or J uncertainties. Decay constants and isotopic abundances after Min et al. (2000).

†Full uncertainties incorporate decay constant uncertainty of Min et al. (2000) and standard uncertainty.

TABLE 5. BEAVER RIM OXYGEN AND CARBON STABLE ISOTOPE RESULTS

Sample	Section	Meter above base	$\delta^{18}O$	$\delta^{18}O/^{16}O$ Std Dev	$\delta^{13}C$	$\delta^{13}C/^{12}C$ Std Dev
1	Sand Draw 1	20	-10.68	0.01	-2.63	0.02
2	Sand Draw 1	65.5	-14.70	0.02	-4.94	0.02
3	Sand Draw 1	89.5	-14.70	0.02	-3.96	0.01
4	Sand Draw 1	105.5	-15.85	0.01	-4.62	0.01
5	Sand Draw 2	11.5	-15.67	0.02	-4.30	0.02
6	Sand Draw 3	1.5	-1.54	0.02	0.93	0.02
7	Sand Draw 3	3.5	-1.36	0.01	1.74	0.01
8	Sand Draw 3	4	-1.53	0.01	2.16	0.02
9	Sand Draw 3	8.5	-5.04	0.03	-1.87	0.02
10	Sand Draw 3	9	-18.63	0.01	-2.66	0.01
11	Sand Draw 3	9.5	-2.22	0.03	-0.68	0.01
12	Sand Draw 3	10	-15.06	0.02	-2.52	0.03
13	Sand Draw 3	12	-17.64	0.01	-3.06	0.01
14	Sand Draw 3	12.5	-14.58	0.02	-4.99	0.01
15	Sand Draw 3	20.5	-9.96	0.02	-1.54	0.01
16	Sand Draw 3	28	-12.81	0.02	-4.63	0.02
17	Sand Draw 3	30	-4.29	0.05	-0.94	0.02
18	Sand Draw 3	33.5	-1.99	0.01	-0.47	0.01
19	Sand Draw 3	35.5	-13.59	0.01	-2.43	0.01
20	Sand Draw 3	39	-10.98	0.03	-4.26	0.01
21	Sand Draw 3	40	-11.85	0.04	-3.38	0.03
22	Sand Draw 3	42	-11.85	0.02	-5.54	0.01
23	Sand Draw 3	45.5	-9.99	0.02	-3.69	0.01
24	Sand Draw 3	47.5	-11.39	0.03	-5.06	0.03
25	Sand Draw 3	50.5	-15.13	0.02	-3.44	0.01
		Average	**-10.33**	**5.44**	**-2.64**	**2.10**

Note. Stable isotope values $\delta^{18}O$ and $\delta^{13}C$ are reported relative to V-PDB, Vienna Pee Dee belemnite, in per mil (‰). The precision for δ18O and δ13C of each sample is ≤0.5‰ and ≤0.4‰, respectively.

TABLE 6. SUMMARY TABLE OF δD (‰) FOR GLASS SAMPLES

Sample	Location	Latitude (°N)	Longitude (°W)	Mean δD (‰)	2σ (‰)	Mean water content (wt %)	2σ (wt %)	Age (Ma)	Full Error (2σ)
W34	East Beaver Rim	42.75603	107.60007	-181.81	1.96	6.12	0.06	46.76	0.17
W33	East Beaver Rim	42.75603	107.60007	-193.96	1.79	6.16	0.1	46.92	0.16
W30	East Beaver Rim	42.76922	107.57624	-168.44	1.1	8.58	0.18	48	-
450WB	West Beaver Rim	42.72426	108.16924	-160.05	0.33	6.14	0.04	39.84	0.16
White Lignitic Tuff	West Beaver Rim	42.71022	108.18227	-83.59	4.73	10.87	0.03	47.7	0.83
444WB	Lysite Mountain	43.57734	107.61180	-108.37	0.35	11.2	0.15	49	-

Note. δD values are reported relative to SMOW. Dates relative to 28.201 Ma Fish Canyon sanidine (Kuiper et al. 2008). Samples W30 and 444WB are best estimate dates.

TABLE 7. PREVIOUSLY PUBLISHED DATED SAMPLES OF THE WAGON BED FORMATION

Sample	Author	Year	Location	Lattitude (°N)	Longitude (°W)	Age (Ma)	Full error (2σ)*	Mineral	Analysis Type
GH17-438B	Gregory and Broes	2018	E Beaver Rim	42.7674	107.59934	48.9	0.9	Zircon	U-Pb
GH17-436A	Gregory and Broes	2018	E Beaver Rim	42.76799	107.59082	48.6	0.5	Zircon	U-Pb
20150925RL-03	Lynds et al.	2016	E Beaver Rim	42.755	107.40821	45.4	0.3	Zircon	U-Pb
20150925RL-05	Lynds et al.	2016	E Beaver Rim	42.79347	107.39160	48.0	0.3	Zircon	U-Pb
White Lignitic Tuff	Smith et al.	2008	W Beaver Rim	42.71022	108.18227	47.7	0.4	Sanidine	$^{40}Ar/^{39}Ar$
Locality 4	Love	1964	Lysite Mountain	43.57328	107.61086	46.2	1.5	Biotite	K/Ar
Ka1018	Evernden et al.	1964	W Beaver Rim	42.71193	108.17265	46.6	1.5	Biotite	K/Ar†
Ka1021	Evernden et al.	1964	W Beaver Rim	42.6128	108.273	50.3	1.8	Biotite	K/Ar†

*Full uncertainties incorporate decay constant uncertainty of Min et al. (2000) and standard uncertainty.

†All K-Ar dates recalibrated to modern decay constants of Min et al. (2000), and are reported relative to Fish Canyon tuff sanidine standard (Kuiper et al., 2008).

TABLE 8. PUBLISHED DATES FOR REGIONAL VOLCANIC SEQUENCES

Sample	Author	Location	Formation	Age (Ma)	Fully propagated uncertainty (2σ)	Mineral	Analysis Type
Upper lava flow groundmass	Feeley and Cosca (2003)	Absaroka Volcanic Province	Trout Peak Trachyandesite	48.37	0.15	Sanidine	$^{40}Ar/^{39}Ar$
Lower lava flow groundmass	Feeley and Cosca (2003)	Absaroka Volcanic Province	Trout Peak Trachyandesite	48.76	0.19	Sanidine	$^{40}Ar/^{39}Ar$
Blue Point ash	Hiza (1999)	Absaroka Volcanic Province	Blue Point Marker	48.10	0.17	Sanidine	$^{40}Ar/^{39}Ar$
2015-0925RL-04	Lynds et al. (2016)	Rattlesnake Hills	Rattlesnake Hills Volcanics	45.20	0.2	Zircon	U-Pb
2016-0802RT-01	Lynds et al. (2016)	Rattlesnake Hills	Rattlesnake Hills Volcanics	45.50	0.2	Zircon	U-Pb
phonolite	Pekarek et al. (1974)	Rattlesnake Hills	Rattlesnake Hills Volcanics	46.04	2.72	Sanidine	K-Ar
rhyodacite	Pekarek et al. (1947)	Rattlesnake Hills	Rattlesnake Hills Volcanics	45.80	1.05	Oligoclase	K-Ar

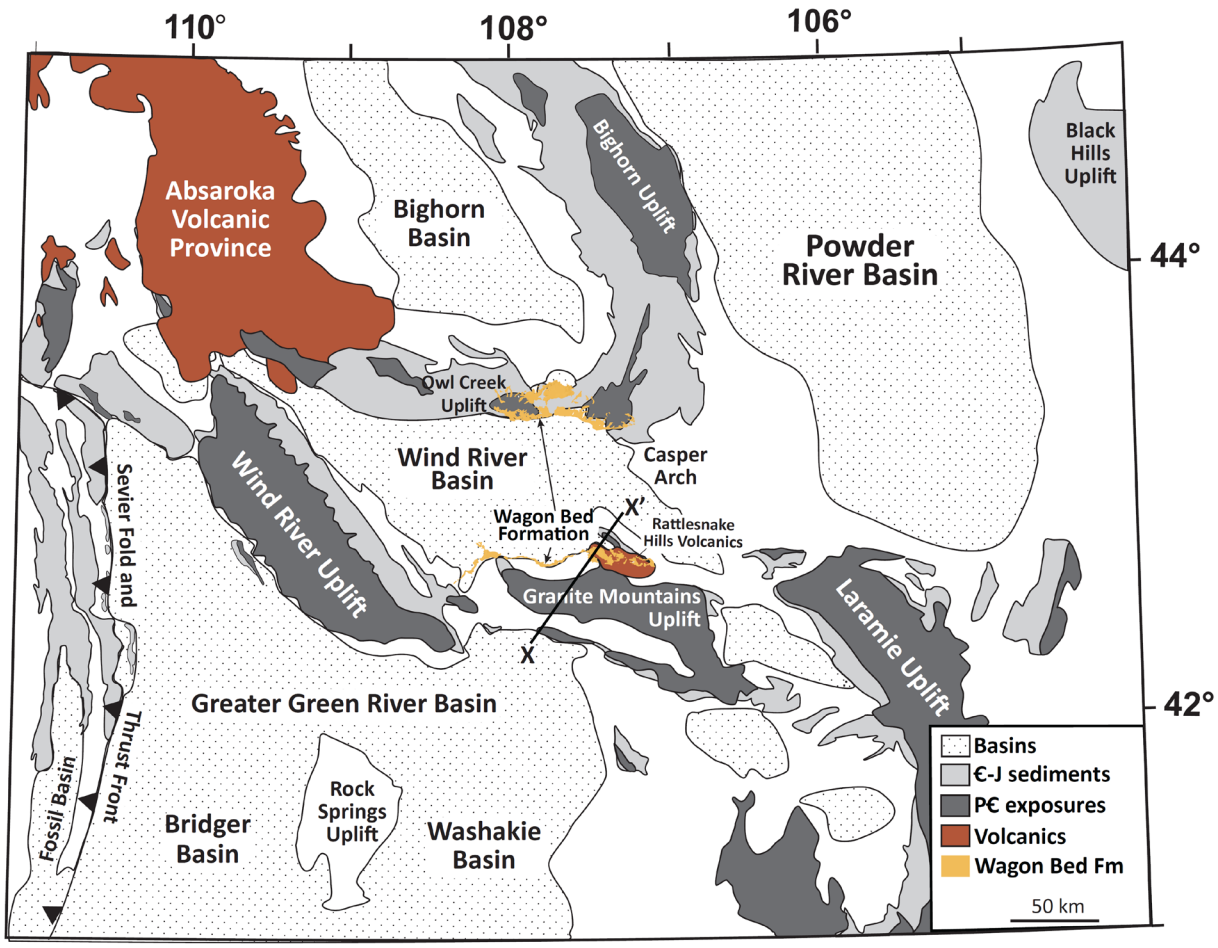

Figure 1. Map showing locations of Laramide uplifts, associated basins, Eocene volcanic provinces, and present day location of the Wagon Bed Formation. Modified from Smith et al. (2008).

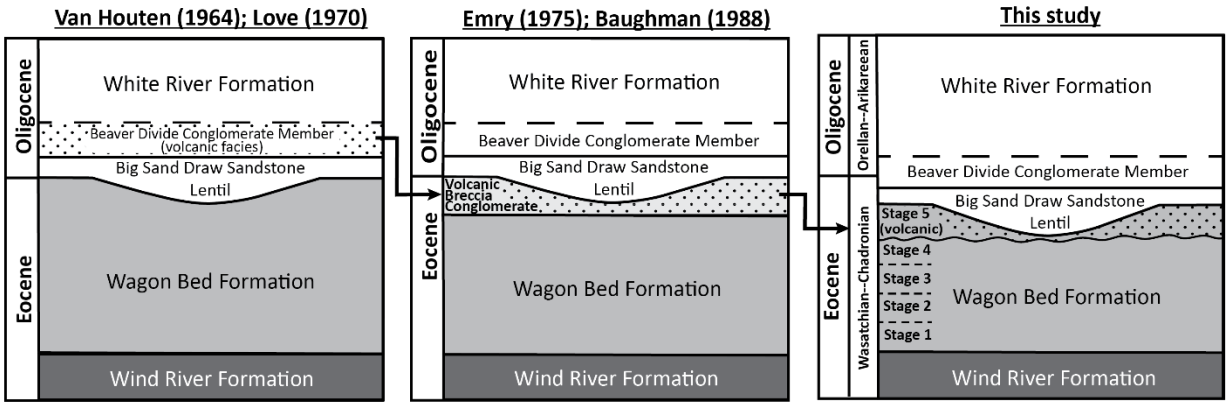

Figure 2. Lithostratigraphic relationships of the Wagon Bed Formation and surrounding formations along the Beaver Rim, as interpreted from multiple studies.

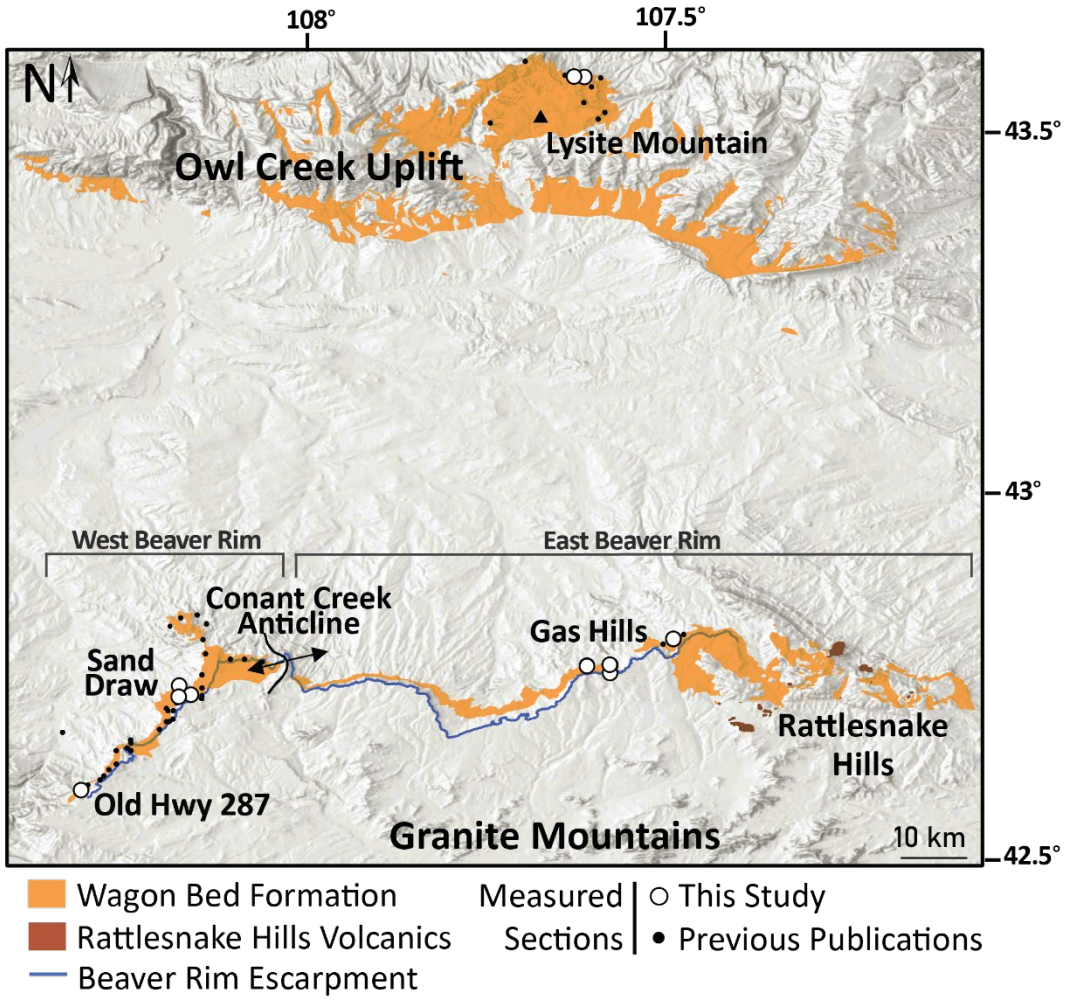

Figure 3. Map of the Beaver Rim and Lysite Mountain areas. Locations of measured sections from this study and previous publications are shown. Sections are from Van Houten (1964), Bay (1969), Baughman (1988), and Amos (1991).

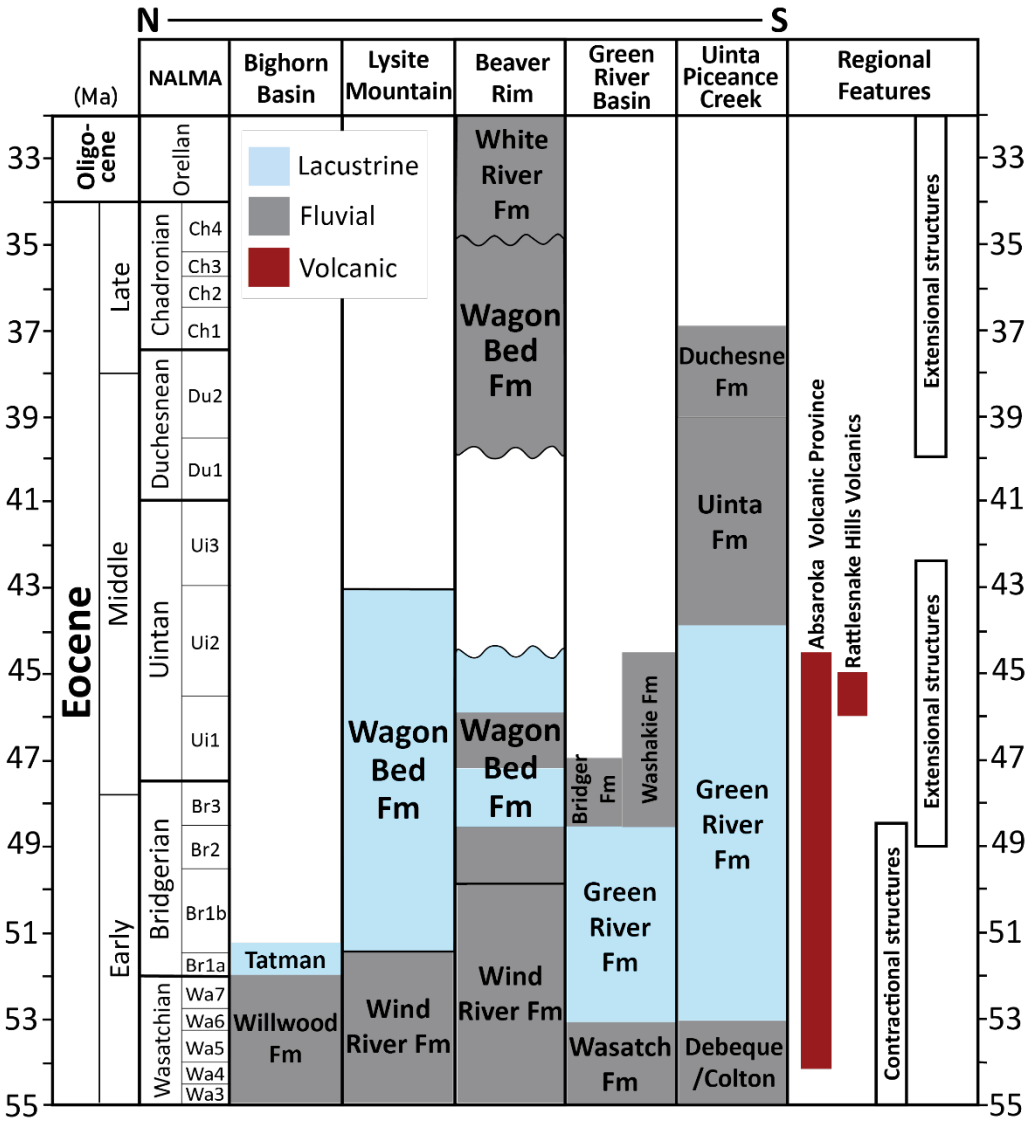

Figure 4. Age comparison of the Wagon Bed Formation to other Eocene formations in nearby basins and to regional features. Data from Evernden et al. (1964); Pekarek (1974); Constenius (1998); Hiza (1999); Feely et al. (1999;2002); Feely and Cosca (2003); Smith et al. (2008); Smith and Carroll (2015); Lynds et al. (2016); Best et al. (2016); Weil et al. (2016); Speijer et al. (2020); Currie and Copeland (2022).

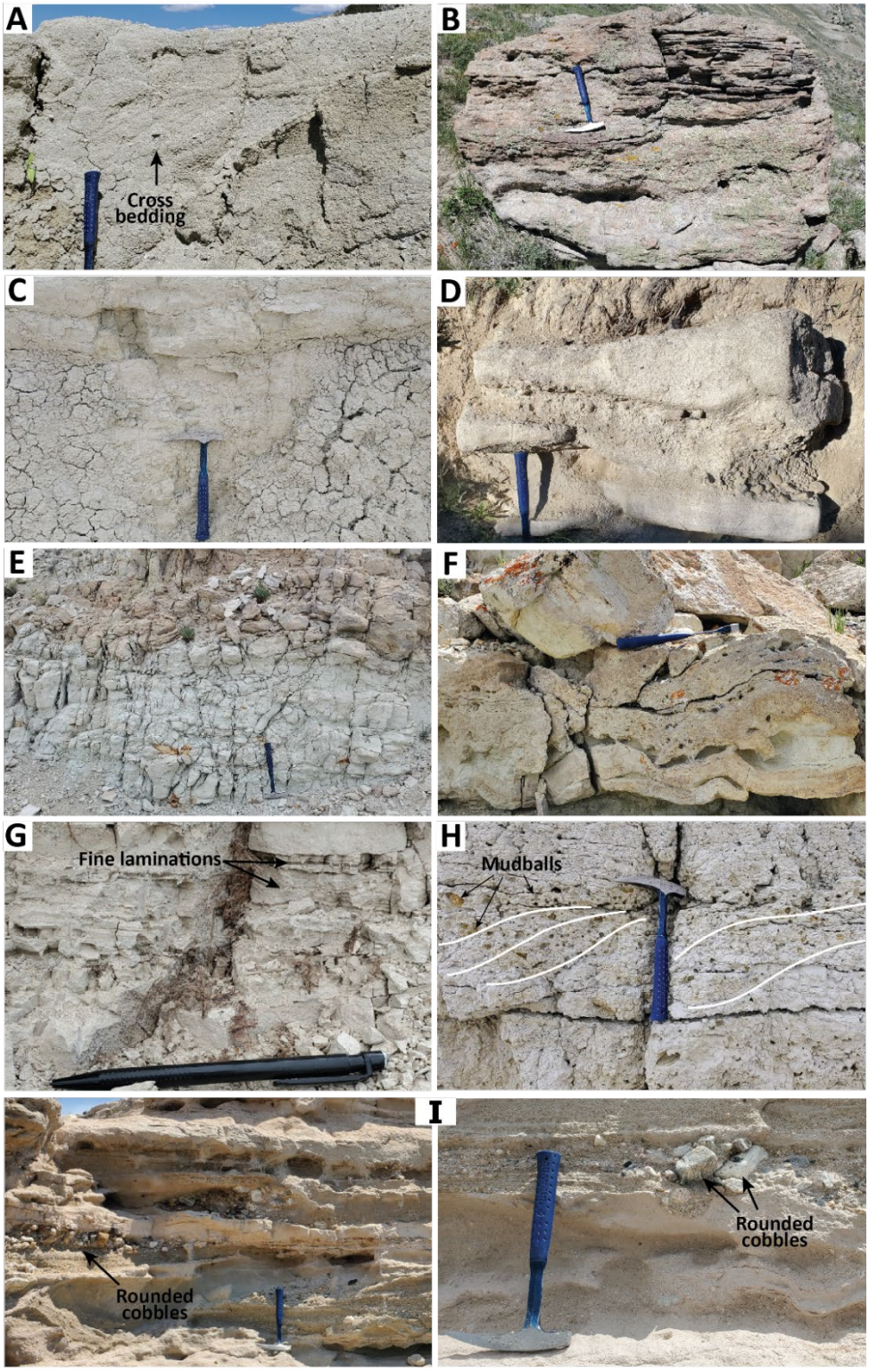

Figure 5. Images of lithofacies. A – tuffaceous sandstone; B – Sandstone; C – tuffaceous mudstone; D – pebble conglomerate; E – carbonate cemented sandstone; F – sandy limestone; G – mudstone; H – intraclastic reworked tuff; I – volcanic pebble conglomerate. Hammer 33 cm and pencil 14 cm for scale.

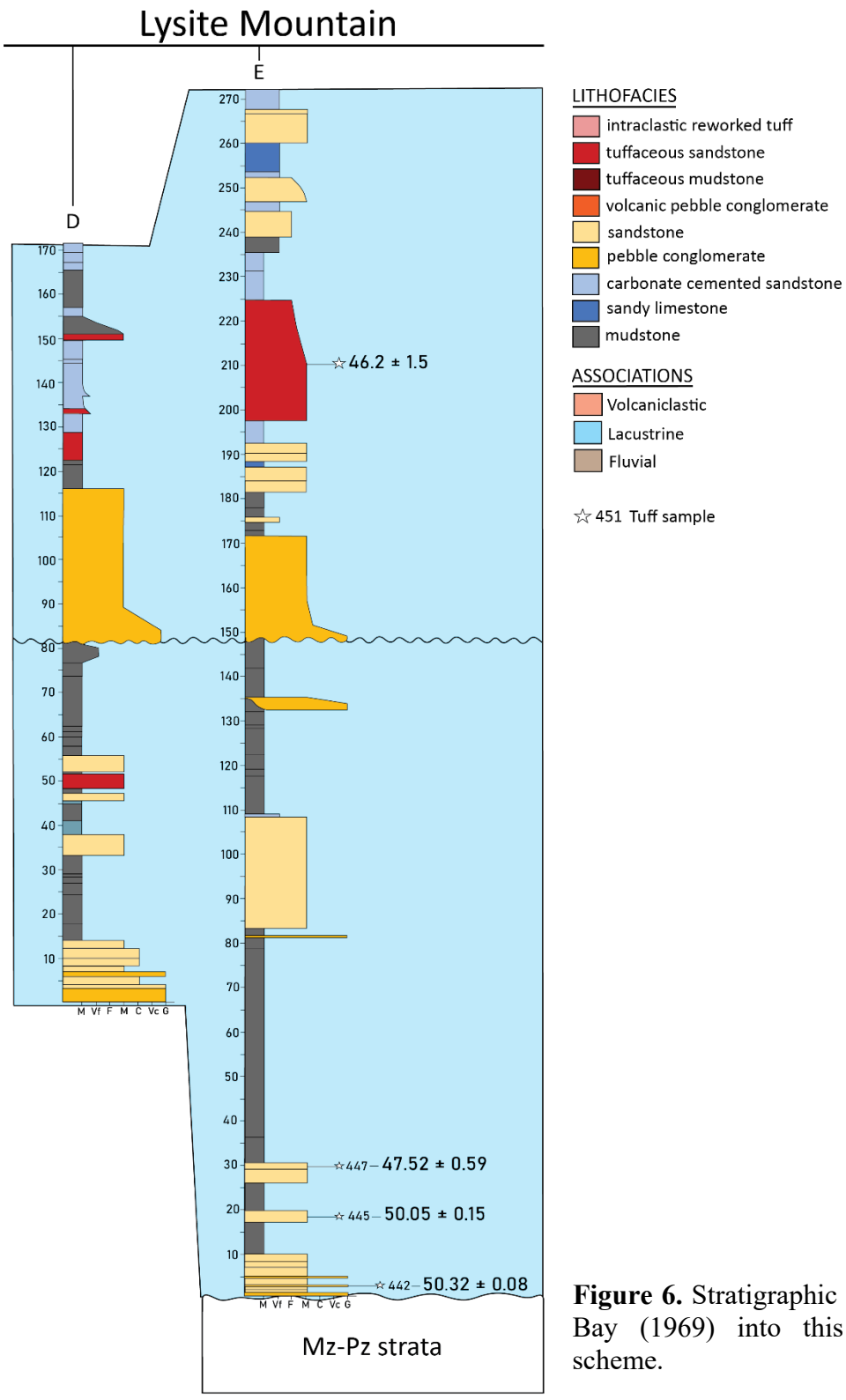

Figure 6. Stratigraphic section adapted from Bay (1969) into this study's lithofacies scheme.

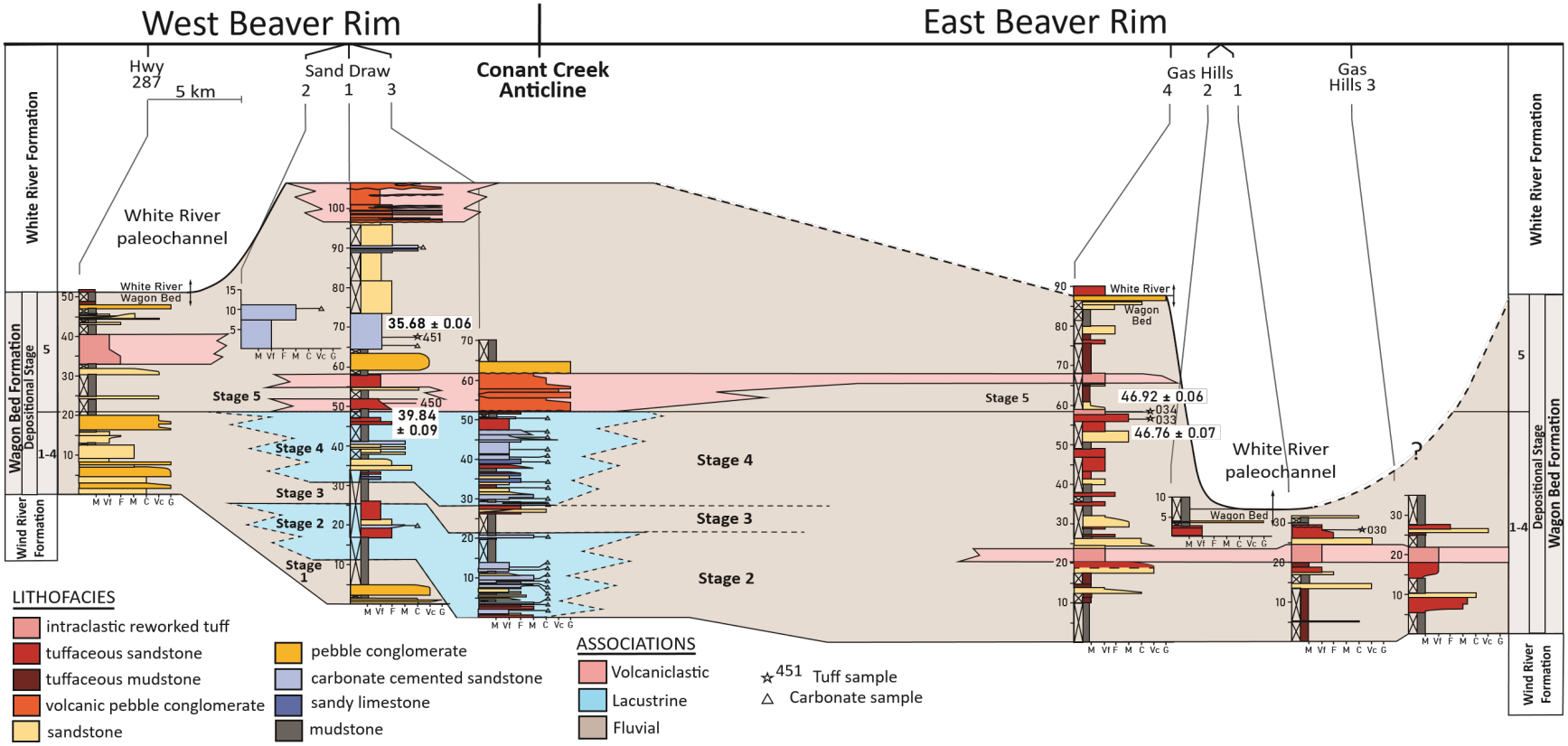

Figure 7. Stratigraphic correlations of 8 measured sections along the Beaver Rim.

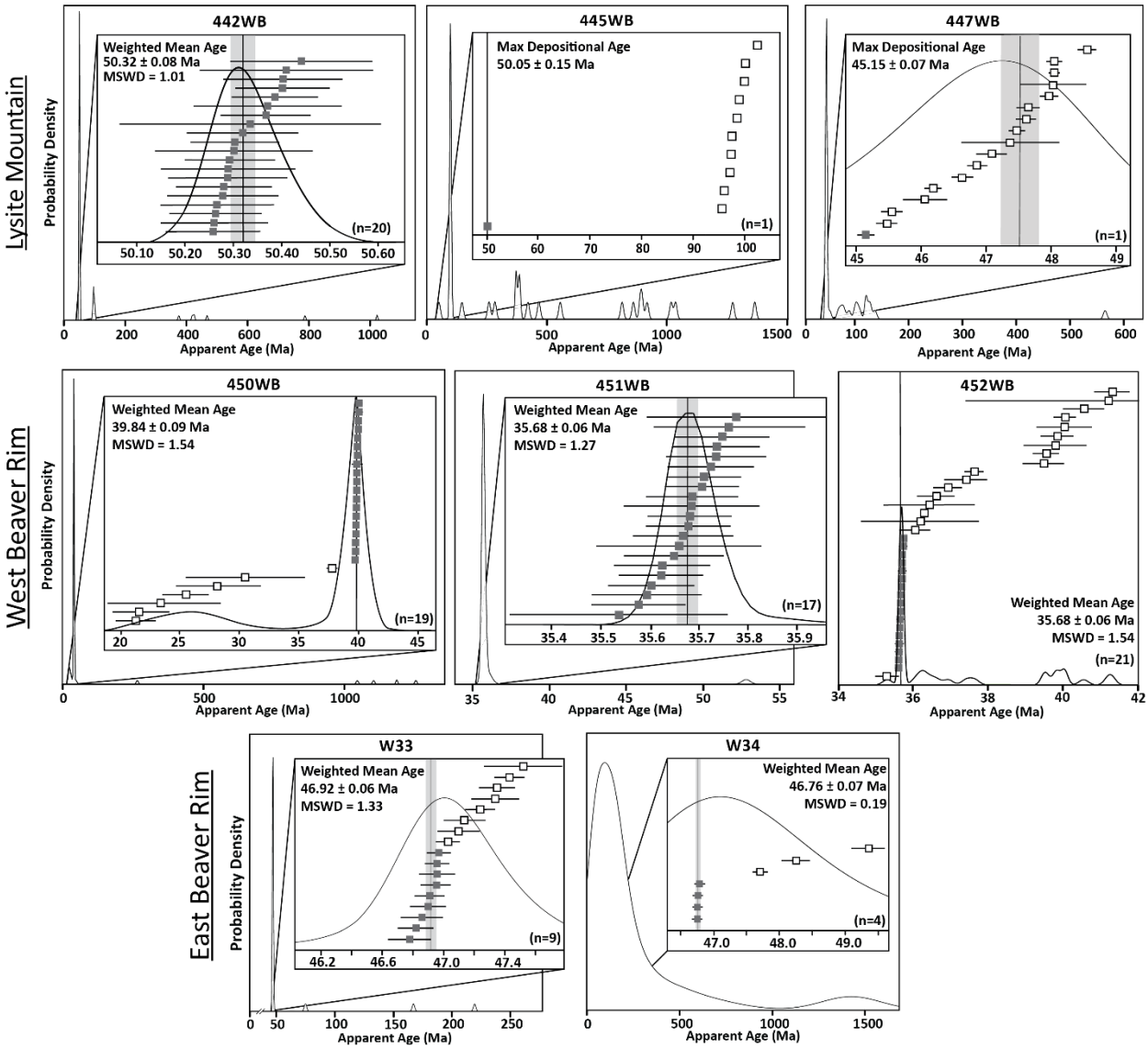

Figure 8. Probability density diagrams showing a summary of $^{40}Ar/^{39}Ar$ results of sanidine from 8 tuffaceous sandstone beds. Samples 442WB, 445WB, and 447WB are from the Lysite Mountain area. Samples 450WB, 451WB, and 452WB are from the west Beaver Rim area, and sample W33 and W34 are from the east Beaver Rim. MSWD = Mean square of weighted deviates.

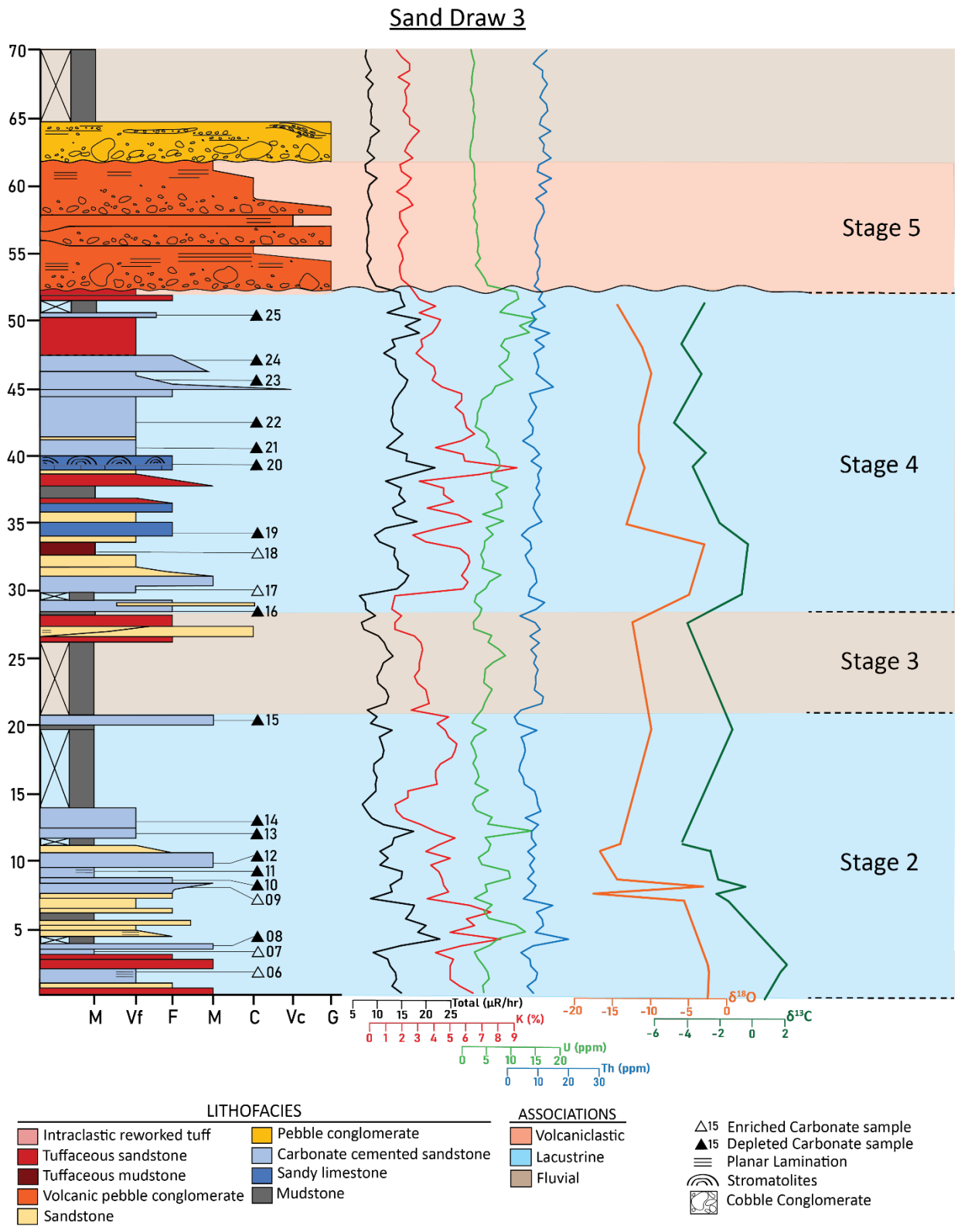

Figure 9. Sand Draw 3 measured section with gamma ray and stable isotope curves.

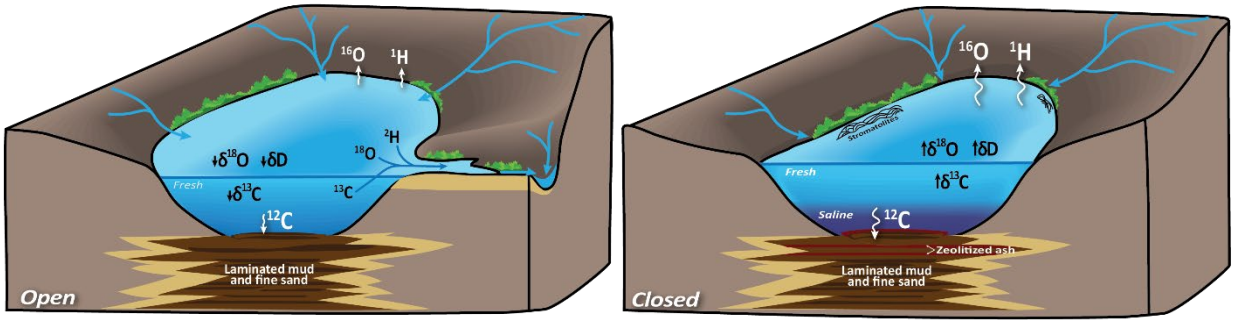

Figure 10. Simplified figure describing the fractionation of oxygen, carbon and hydrogen, and sedimentary processes and features present in a closed or open lacustrine basin.

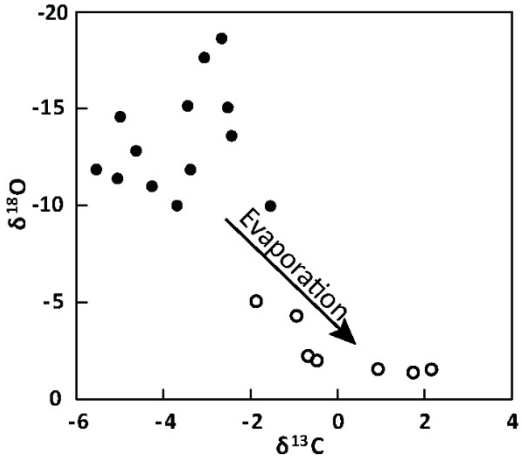

Figure 11. Cross-plot of $\delta^{18}O$ vs. $\delta^{13}C$. Hollow dots are the most enriched, occur in the lowest 10 meters of both lacustrine intervals, and correspond to samples 6, 7, 9, 11, 17, and 18.

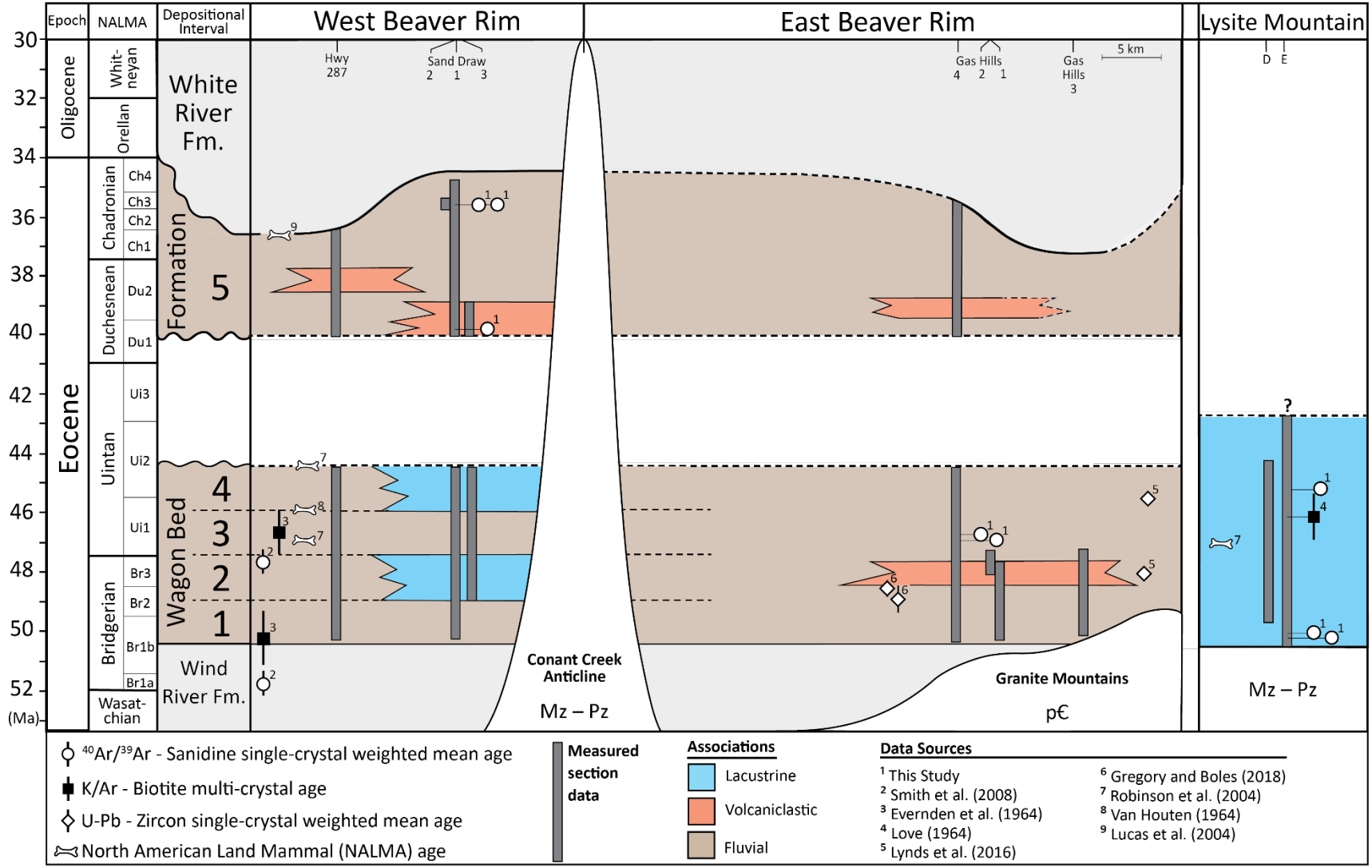

Figure 12. Chronostratigraphic figure showing the timing of Wagon Bed Formation deposition and other relevant formations along the Beaver Rim and at Lysite Mountain. Radioisotopic ages, biostratigraphy, approximate correlations, and depositional intervals are shown. All radioisotopic ages are reported according to Kuiper et al. (2008) Fish Canyon tuff using decay constants of Min et al. (2001) and are shown with 2σ full uncertainties. Samples without error bars have error less than the width of the shape.

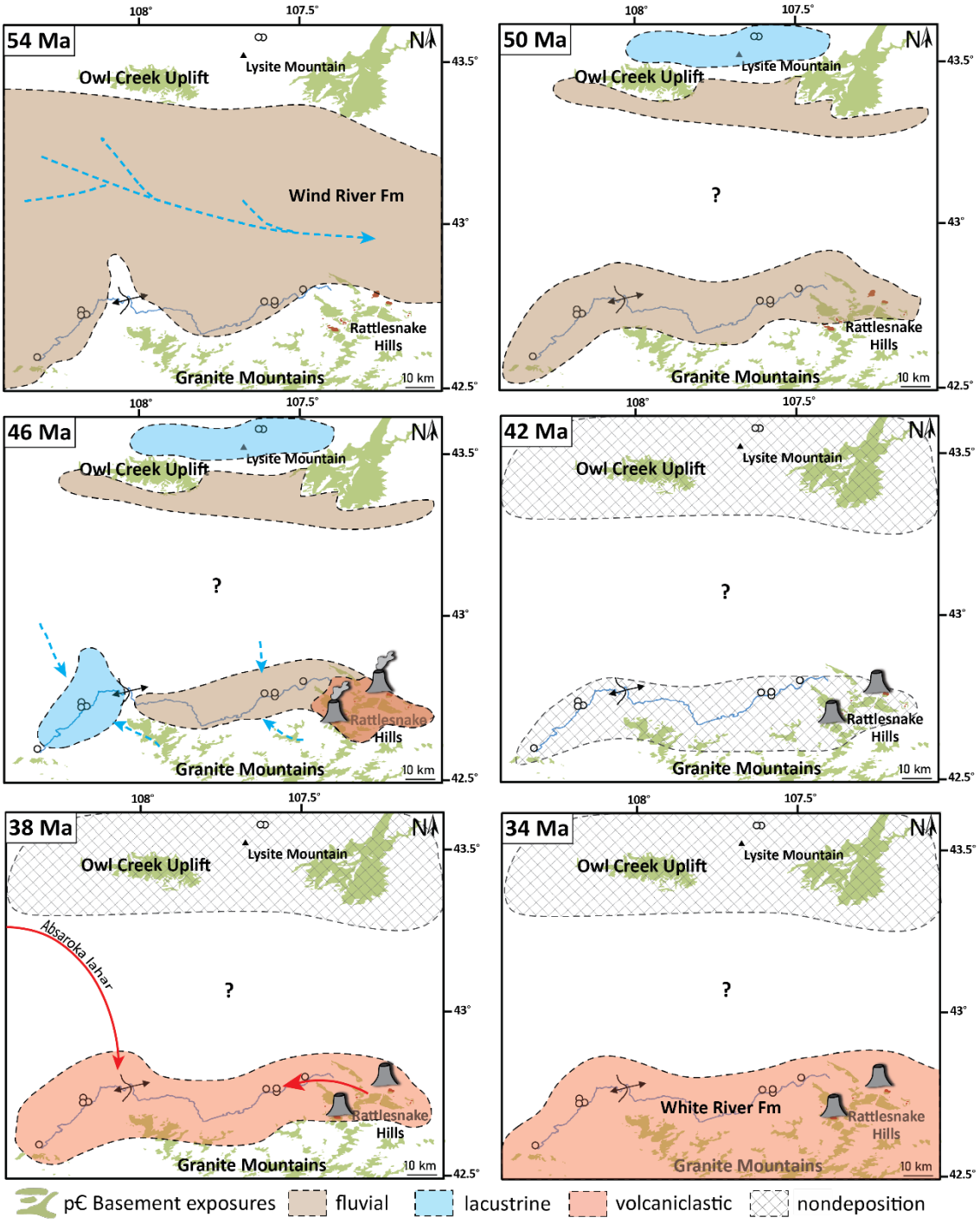

Figure 13. Synoptic paleogeographic maps for Wagon Bed Formation deposition for Lysite Mountain and Beaver Rim areas.

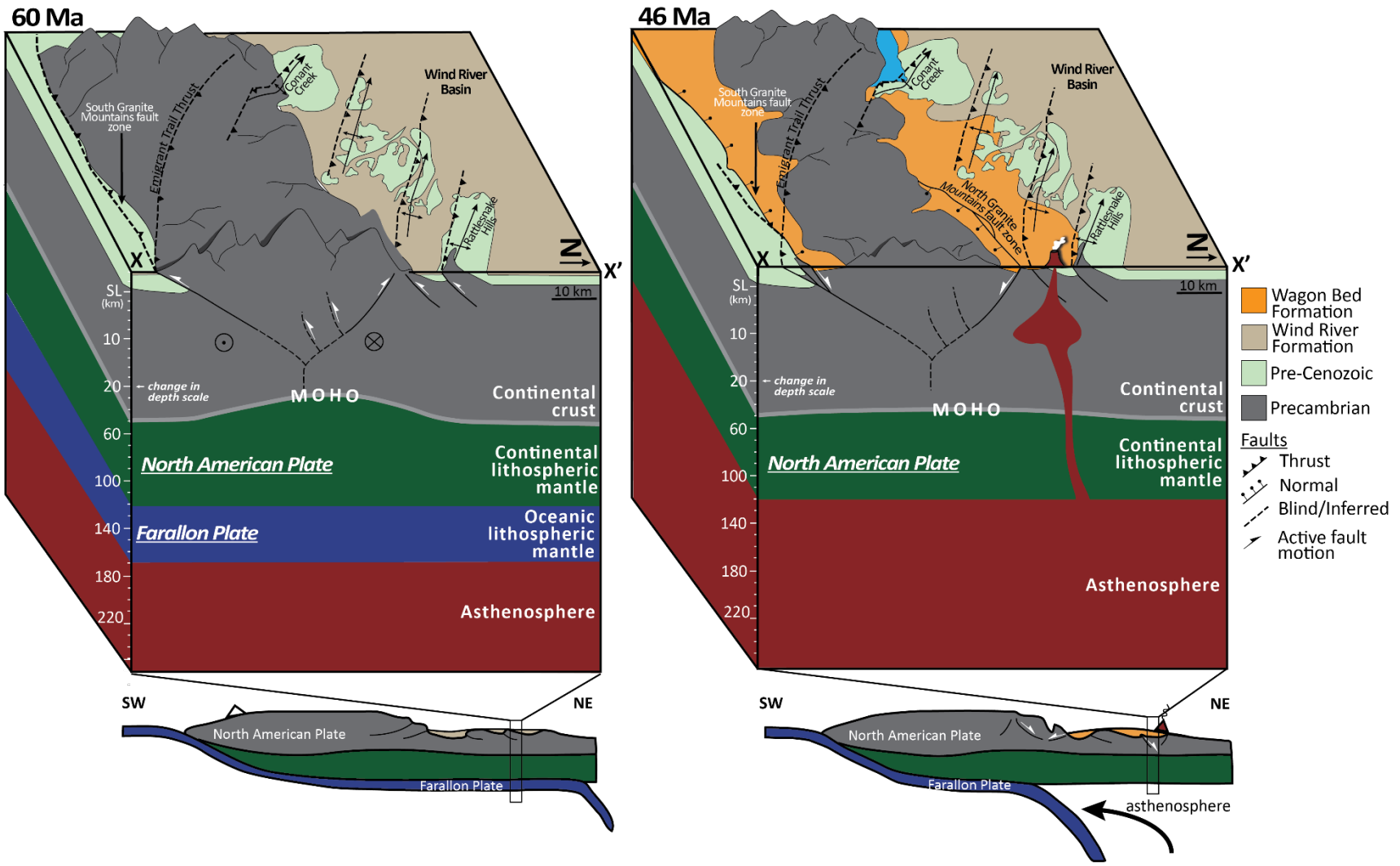

Figure 14. Model for proposed collapse of the Granite Mountains, and in fill of the Wagon Bed Formation. X-X' cross section line is located on Figure 1. No vertical exaggeration. Adapted from Weil et al. (2016).